Ore Geology Reviews 106 (2019) 351–368

Contents lists available at ScienceDirect

Ore Geology Reviews

journal homepage: www.elsevier.com/locate/oregeorev

Magmatic oxidation state of the Baogutu porphyry copper deposit in the west Junggar of China: Implication for ore-formation

Shaoni Wei[a,b], Yongfeng Zhu[b,*], Jiuyang Jiang[b], Wanyi Feng[b]

[a] College of Geology and Environment, Xi'an University of Science and Technology, Xi'an 710054, China
[b] The Key Laboratory of Orogenic Belts and Crustal Evolution, School of Earth and Space Sciences, Peking University, Beijing 100871, China

ARTICLE INFO

Keywords:
Magmatic oxidation state
Porphyry copper deposit
Baogutu
Xinjiang

ABSTRACT

The ore-forming processes in the Baogutu porphyry copper deposit are spatially and temporally related to the Late Carboniferous intrusions in the west Junggar of China. The mineralized intrusions, consisting of granodiorite, quartz diorite, and diorite, are characterized by moderate zircon Ce^{4+}/Ce^{3+} ratios (15.9–163) and Eu/Eu^* ratios (0.25–0.57; $Eu/Eu^* = Eu_N/(Sm_N \times Gd_N)^{1/2}$). Estimated magmatic oxidation state based on amphibole crystallized in the deep magma chamber ($\log fO_2 = \triangle FMQ + 1.7$) is lower comparing with that based on amphibole crystallized in the shallow magma chamber ($\log fO_2 = \Delta FMQ + 3.5$). The Baogutu ore-forming magmas were moderately oxidized with an average $\log fO_2$ value of $\Delta FMQ + 2.5$ (based on amphibole oxygen-barometer) or $\Delta FMQ + 2.7$ (based on magnetite – ilmenite oxygen-barometer). These data indicate that the Baogutu ore-forming magmas were moderately oxidized.

1. Introduction

The oxidation states of magmatic system play a crucial role in the formation of large porphyry copper deposits (Mungall, 2002; Richards, 2003; Sun et al., 2013). Porphyry copper deposits are usually formed in relatively oxidized magmatic systems with $\log fO_2$ values varying between the hematite-magnetite (HM) and nickel-nickel oxide (NNO) buffers, mostly exceeding $\Delta FMQ + 2$ (FMQ represents the fayalite–magnetite–quartz buffer) (Jugo et al., 2005; Hattori, 2018). The mineralized intrusions are mainly magnetite-series I-type granitoids (Jenner et al., 2010; Sillitoe, 2018) and contain highly oxidized minerals such as primary anhydrite and hematite (Hattori and Keith, 2001; Stern et al., 2007; Grondahl and Zajaca, 2017). Magmatic sources with high oxidation state would breakdown the magmatic sulfide phases (S^{2-}), and ensure that sulfate (SO_4^{2-}) is the dominant sulfur species in the melt (Carroll and Rutherford, 1988; Jugo et al., 2010). This process likely releases large amounts of chalcophile elements and Au to the melt, which can transport these ore-forming metals to the shallow crust (Richards, 2009; Nadeau et al., 2010; Botcharnikov et al., 2011; Wilkinson, 2013). Hence, most ore-forming magmas of large porphyry copper deposits show relatively high $\log fO_2$ values. Examples include the El Teniente in Chile (Cannell et al., 2005), the Oyu Tolgoi in Mongolia (Khashgerel et al., 2006, 2008) and the Yulong in China (Hou et al., 2003; Liang et al., 2009). However, a few reduced porphyry copper deposits with $\log fO_2$ values lower than or equal to the FMQ buffer have been recognized (Randall et al., 1994; Rowins et al., 1997; Smith et al., 2012). These deposits contain hypogene magmatic pyrrhotite and are associated with ilmenite-bearing granitoids (Rowins, 2000). Examples of such deposits include the 17 Mile Hill in Australia (Rowins et al., 1997), the San Anton in Mexico (Randall et al., 1994) and the Catface in Canada (Smith et al., 2012).

The Baogutu porphyry copper deposit, located in the south part of the west Junggar of China, is medium-sized in copper reserve (Zhang et al., 2006a). Extensive researches mainly based on geology, alteration, mineralization and geochronology have been performed on the Baogutu porphyry copper deposits (Zhang et al., 2006b; Shen et al., 2009; Wei and Zhu, 2015). However, the oxidation state of the ore-forming magma and its relationship with copper mineralization remain controversial. Cao et al. (2014) suggested that the mineralized intrusions are ilmenite-series granitoids with $\log fO_2$ values between $\Delta NNO + 0$ and $\Delta NNO - 2$. In contrast, Shen and Pan (2015) reported that the ore-bearing diorite contains magmatic magnetite with $\log fO_2$ values $> \Delta FMQ + 1$. Cao et al. (2017) estimated the $\log fO_2$ values of the ore-bearing granitoids and identified two distinct results: $\log fO_2 = \Delta NNO + 0.6$ and $\log fO_2 < \Delta NNO$. Zhu et al. (2018) suggested two magmatic stages: the early oxidized stage ($> \Delta NNO + 2.4$) and the late reduced stage ($< \Delta NNO - 0.6$). Here, we use mineral compositions (magnetite, ilmenite, amphibole, zircon) and

---

[*] Corresponding author.
E-mail address: yfzhu@pku.edu.cn (Y. Zhu).

https://doi.org/10.1016/j.oregeorev.2019.02.018
Received 14 May 2018; Received in revised form 7 January 2019; Accepted 14 February 2019

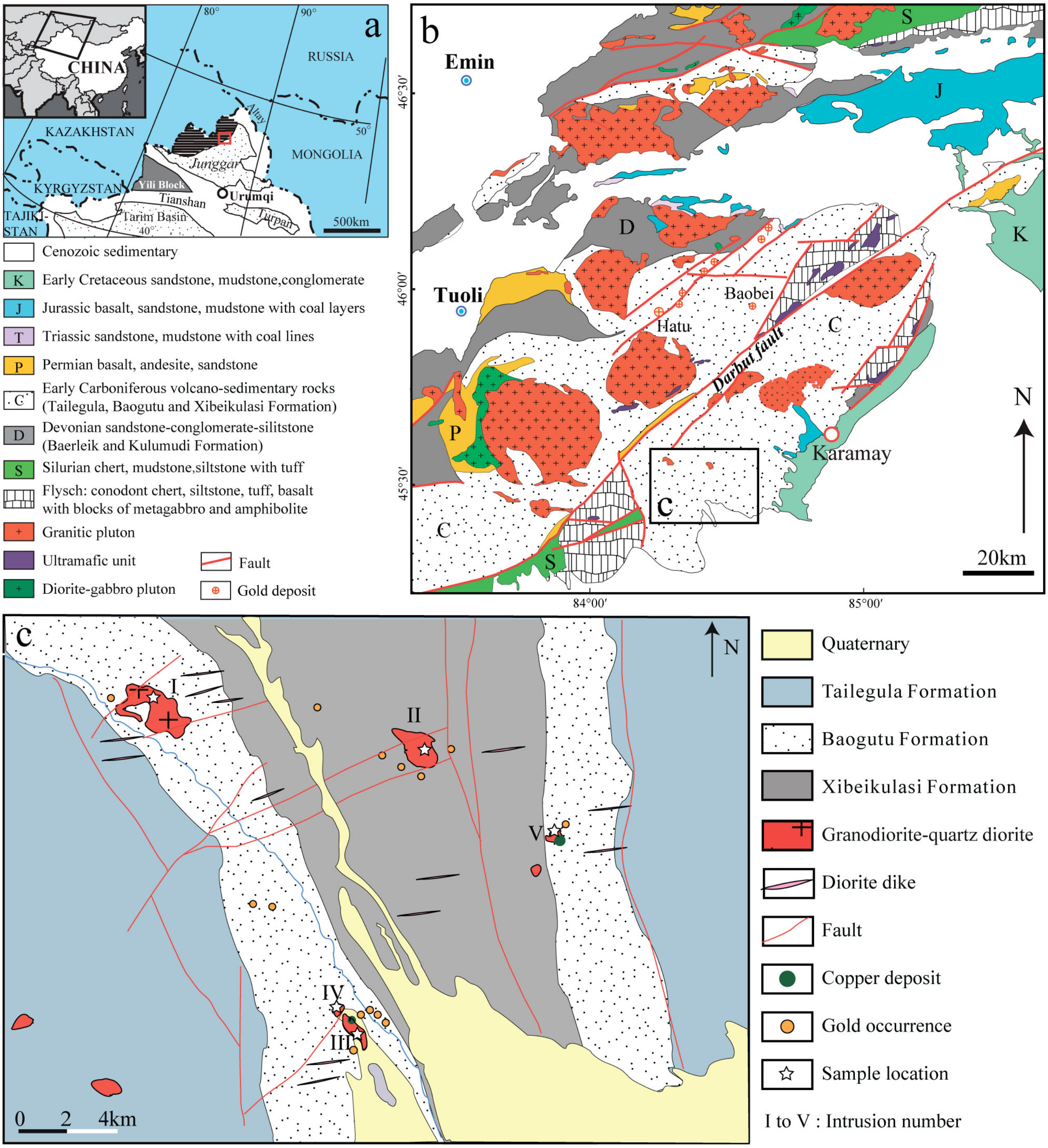

Fig. 1. (a–b) Simplified geological map of the west Junggar (modified from Zhu et al., 2013). (c) Geological map of the Baogutu region (modified after Zheng et al., 2015) showing occurrences of the studied intrusions with sample locations.

geochemistry of the Baogutu intrusions to determine the oxidation state of ore-forming magmas, which contributes to understanding of the ore-forming processes of porphyry copper deposits.

2. Regional geology

The west Junggar is a major constituent of the central Asian metallogenic domain (Fig. 1; Zhu et al., 2016). It extends westward to the Junggar–Balkhash region in Kazakhstan. Several ophiolite mélange belts are distributed in the west Junggar, striking NE or EW, from northwest to southeast including Barleik, Mayile, Tangbale, Dalabute, Hongguleleng, and Karamay with ages ranging from Cambrian to Devonian (Zhu and Xu, 2006; Chen and Zhu, 2011; Xu et al., 2012; Yang et al., 2013; Zhu et al, 2015). Flysch, consisting of siltstone, mudstone, tuff and chert, overlies the ophiolite mélanges. The ophiolite mélanges and associated flysch underwent intensive deformation and were unconformably covered by the Late Paleozoic volcanic– sedimentary units (Zhu et al., 2013).

Early Carboniferous volcanic–sedimentary strata consist of three stratigraphic units: Tailegula, Baogutu and Xibeikulasi Formations (Fig. 1b–c). The Tailegula Formation contains tuffaceous siltstone, tuff, basalt and siliceous units. The zircon SHRIMP age of the tuff was 328.1 ± 1.8 Ma (Wang and Zhu, 2007). The Baogutu Formation is composed of coarse-grained tuffaceous sandstone, fine-grained sandstone, siltstone and tuff. Zircons separated from the tuff gave ages of 328–342 Ma (An and Zhu, 2009; Zhu et al., 2014). The Xibeikulasi Formation is mainly composed of coarse-grained tuffaceous sandstone with tuff, tuffaceous siltstone and andesite interlayers.

Late Paleozoic granitic plutons are widely distributed, intruding into the ophiolite mélanges and early Carboniferous volcanic–sedimentary strata, with an age peak of 310–290 Ma (Zhu et al., 2013). The dioritic to granitic porphyries and dykes are mainly exposed in the Baogutu region. They intruded into the early Carboniferous volcanic–sedimentary strata during 320–310 Ma (Liu et al., 2009; Wei et al., 2011). The gabbroic to dioritic dykes, intruding into volcanic–sedimentary units and granitic plutons, were dated to be 280–240 Ma (Li et al., 2004; Yin et al., 2013). The granitic plutons and gabbroic to dioritic dykes were suggested to be the products of post-collisional magmatism (Han et al., 2006; Jiang and Zhu, 2018).

Numerous copper–gold deposits have been discovered in the west Junggar. For example, the Hatu–Sartohay Au concentration area, located in the north side of the NE-striking Darbut fault, contains more than ten gold deposits (Fig. 1b, Qiu and Zhu, 2015; Wang and Zhu, 2015; Zhang and Zhu, 2016). The Baogutu Cu–Au concentration area, located in the south side of the Darbut fault, contains one porphyry copper deposit, one gold deposit and more than ten gold occurrences (Fig. 1c, An and Zhu, 2010). The Baogutu porphyry copper deposit is hosted in granitic to dioritic stocks, while the gold mineralization occurs in the contact zone between stocks and early Carboniferous volcanic–sedimentary units (Song et al., 2007; Zheng et al., 2015).

3. Geology of the Baogutu copper deposit

The Baogutu porphyry copper deposit, with resources of 225 Mt at average grades of 0.28 wt% Cu, 0.01 wt% Mo and 0.14 g/t Au, is located in the south side of the Darbut faults (Zhang et al., 2006a). The Xibeikulasi, Baogutu and Tailegula Formations formed a SN-trending fold structure. Several mineralized intrusions (numbered as I to V) emplaced into the core of the fold (Figs. 1c, 2a–b). These intrusions are mainly granodiorite, quartz diorite and diorite. They display similar trace element geochemical and Sr–Nd–Pb–Hf isotopic signatures (Shen et al., 2009; Tang et al., 2010; Zhu et al., 2014; Wei and Zhu, 2015; Cao et al., 2016). Zircons separated from these intrusions were dated to be 310 Ma to 320 Ma (Liu et al., 2009; Wei et al., 2011).

Different intrusions show distinct alteration and mineralization features. The intrusions I, II and IV are weakly altered and mineralized, bearing only a small amount of disseminated pyrite and chalcopyrite. In comparison, the intrusion III developed remarkable mineralization, and malachite is widespread on its surface. Sulfides including pyrite, chalcopyrite and pyrrhotite, with trace amounts of arsenopyrite, molybdenite, bornite, tetrahedrite, sphalerite, gudmundite and electrum are disseminated in the intrusion and the adjacent wall rocks. However, the ore grade is much lower than the marginal grade. The intrusion V contains a predominance of disseminated Cu–Mo–Au mineralization together with lesser amounts of vein-type and breccia-type mineralization. This intrusion was strongly affected by potassic, propylitic and phyllic alteration. Abundant hydrothermal biotite occurs in the center of the deposit and is locally overprinted by phyllic alteration. The propylitic alteration surrounds the potassic zone and contains weak copper mineralization. Molybdenite separated from the ore body was dated to be 310.4 ± 3.6 Ma using Re–Os method (Song et al., 2007).

4. Petrology of the Baogutu intrusions

The petrographic characteristics of the mineralized intrusions in the Baogutu area were gained based on observations from outcrops and 8 drill holes. These intrusions mainly consist of granodiorite, quartz diorite and diorite, with a small amount of pyroxene diorite. They show equigranular or porphyritic texture, and are mainly composed of plagioclase, amphibole, biotite, K-feldspar, quartz and clinopyroxene (Fig. 2). Accessory minerals include magnetite, ilmenite, sphene, apatite and zircon. Plagioclase, which is the most abundant primary mineral (40–60 vol%), is subhedral to euhedral. Euhedral plagioclase is usually white-colored with polysynthetic twins (Fig. 2c). Some plagioclase crystals show oscillatory zonation. Amphibole (5–15 vol%) coexists with plagioclase (Fig. 2d). Biotite (5–10 vol%), K-feldspar (10–15 vol%) and quartz (5–25 vol%) coexist with plagioclase and amphibole (Fig. 2e). Pyroxene diorite is rarely found in drill holes. Clinopyroxene is replaced by amphibole along rims (Fig. 2f).

Accessory minerals occur as inclusions in amphibole and biotite, or as interstitial crystals between amphibole, plagioclase and biotite. The occurrences of magnetite and ilmenite in different intrusions are distinct. In the intrusions I and II, more magnetite was observed than ilmenite. Both of them coexist with amphibole and plagioclase (Fig. 2g). Ilmenite is more popular in the intrusions III and IV, where magnetite is absent (Fig. 2h). The intrusion V contains more ilmenite than magnetite. Both ilmenite and magnetite occur as inclusions in amphibole and biotite.

5. Analytical methods

Compositions of minerals were determined using an electron probe microanalyzer (EPMA) JXA-8230. Instrument was operated at an acceleration voltage of 15 kV, beam current of 10nA and beam diameter of 1 μm. Standards of natural and synthetic phases were supplied by SPI Company. The ZAF correction method was used for standardization. The analytical precision was better than 1%.

The least altered samples were selected for major and trace element analyses. Whole rock samples were carefully washed by distilled water and crushed into powder, with a grain size of approximately 80 μm. Major element oxides were analyzed using RIX-2100 X-ray fluorescence (XRF) spectrometer. Analytical uncertainty ranged from ± 1% to ± 5%. The FeO analysis was undertaken by titration in order to determine whole-rock Fe^{3+}/Fe^{2+} ratios. The precision of the analyses was generally $< 3\%$. Trace elements were analyzed by inductively coupled plasma mass spectrometry (ICP-MS). For quality control, the standard and parallel samples were analyzed during all analytical runs. The precision of the analyses was generally $< 7\%$ for trace elements.

Zircons were separated from the least altered samples by hand-picking. The zircons were mounted in epoxy and polished to reveal their interiors. CL images show clearly magmatic zones without obvious alteration, suggesting that they were crystallized from magmas. Zircon analyses were performed at Northwest University in Xi'an. A Compex 102 ArF excimer laser system was used to ablate the zircons and standards, and ablated material was carried by He–Ar gas (flowrates of 0.67 L He/min and 0.85 L Ar/min) to an Agilent 7500a ICP-MS. Laser ablation spot sizes were approximately 44 μm. Data were acquired for 20 s with the laser off and 45 s with the laser on, and then the system was flushed with He–Ar gas for 25 s with the laser off. Each block of 8 zircon analyses was bracketed by analysis of standard glass NIST 610, which was used to correct for mass bias drift (Pearce et al., 1997). Calibration was conducted by GLITTER (version 4.0, Macquarie University), assuming SiO_2 to be stoichiometric in zircon ($ZrSiO_4$) with a concentration of ca. 32.78 wt%.

6. Results

6.1. Mineral chemistry

The compositions of primary plagioclase, amphibole, biotite, clinopyroxene, magnetite and ilmenite in the Baogutu intrusions were analyzed with EPMA. Representative chemical compositions are listed in Supplementary Table 1. Plagioclase exhibits a slightly wide range from $An_{14}Ab_{85}Or_1$ to $An_{64}Ab_{35}Or_1$ (Fig. 3a; Supplementary Table 1A). Amphibole is magnesiohornblende based on the classification of Leake et al. (1997), and its $Mg^{\#}$ ($Mg^{\#} = Mg/(Mg + Fe)$) values range from

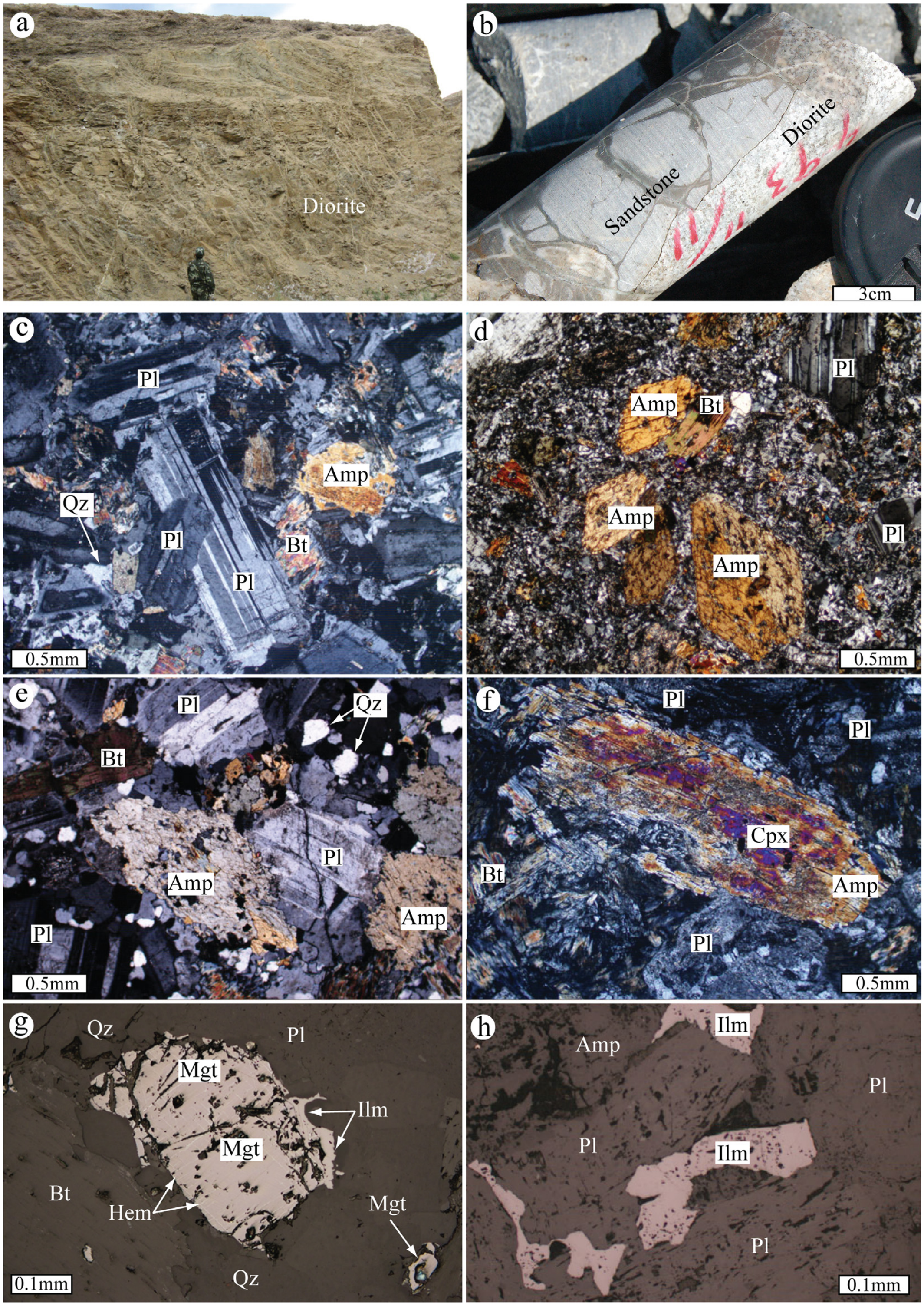

Fig. 2. Outcrop and microphotographs of the Baogutu intrusions. (a) Outcrop of the Baogutu intrusion V. (b) A drill hole sample shows the boundary of diorite intruded sandstone. (c) Diorite from the intrusion III, with plagioclase, amphibole and biotite, cross-polarized light. (d) Granodiorite porphyry from the intrusion II with plagioclase, amphibole and biotite phenocrysts, cross-polarized light. (e) Granodiorite from the intrusion II with plagioclase, amphibole and biotite, cross-polarized light. (f) Pyroxene diorite from the intrusion III with clinopyroxene replaced by amphibole, cross-polarized light. (g) Coexisting magnetite and ilmenite in granodiorite (from the intrusion II); magnetite replaced by hematite along crystal lattice, reflected light. (h) Ilmenite in quartz diorite (from intrusion III), reflected light. Abbreviations: Amp = amphibole, Bt = biotite, Cpx = clinopyroxene, Hem = hematite, Ilm = ilmenite, Mgt = Magnetite, Pl = plagioclase, and Qz = quartz.

0.58 to 0.90 (Supplementary Table 1B, Fig. 3b). Biotite is classified as Mg-biotite using the discrimination diagrams of Foster (1960) (Fig. 3c). It is homogeneous in composition with Mg$^{\#}$ values of 0.40 – 0.65 (Supplementary Table 1C, Fig. 3d). The compositions of clinopyroxene from the diorite are relatively homogeneous, ranging from $En_{37}Fs_{17}Wo_{46}$ to $En_{48}Fs_{10}Wo_{42}$ and corresponding to augite (Fig. 3e) with Mg$^{\#}$ values of 0.69 – 0.87, Al_2O_3 contents of 0.33 – 4.52 wt% and TiO_2 contents of 0.08 – 0.71 wt% (Supplementary Table 1D). According

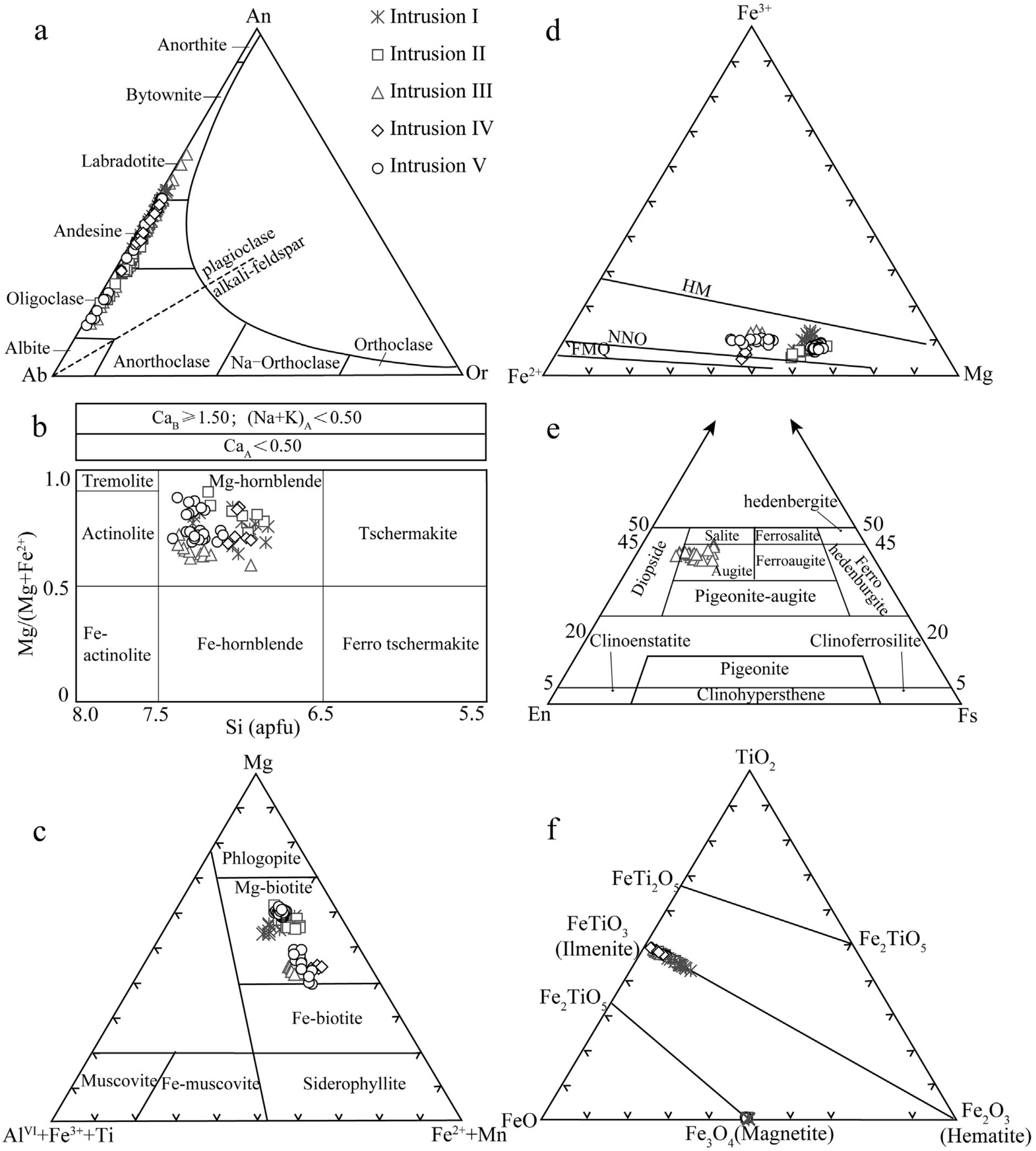

Fig. 3. Compositions of minerals in the Baogutu intrusions. (a) Classification diagram of plagioclase. (b) Classification diagram of calcic amphibole (after Leake et al., 1997). (c) Component diagram of biotite (after Foster, 1960). (d) Fe^{3+}–Fe^{2+}–Mg diagram (Wones and Eugster, 1965), biotite plotting in the field between the Ni–NiO (NNO) and Fe_2O_3–Fe_3O_4 (HM). (e) The plot of Wo–En–Fs for pyroxene. (f) Classification diagram of Fe-Ti oxides (Buddington and Lindsley, 1964).

to the Fe-Ti oxide classification of Buddington and Lindsley (1964), all ilmenite analyses are close to the $FeTiO_3$ end-member with high TiO_2 contents (46.09 – 52.19 wt%). Magnetite analyses are close to the Fe_3O_4 end-member with FeO^T contents of 88.79 – 93.93 wt% (Fig. 3f, Supplementary Table 1E).

6.2. Whole-rock geochemistry

Major element compositions of whole-rock samples from the Baogutu I to V intrusions are variable, with SiO_2 contents ranging from 51.69 wt% to 66.51 wt% (Table 1, Fig. 4a) with an average Na_2O/K_2O ratio of 2.97. Most samples are classified as calc-alkaline series based on the SiO_2 – K_2O diagram (Fig. 4b). All samples have high MgO contents (1.11 – 5.89 wt%) and $Mg^{\#}$ values (0.35 – 0.71). In comparison, geochemical characteristics of most trace elements are similar (Table 1, Fig. 5). They are characterized by enrichments of Cs, Ba, and U, and depletions of Nb, Ta, and Ti. The total REE concentrations of various intrusions vary from 38.3 ppm to 103 ppm. They show moderate enrichments in light REE ($(La/Yb)_N$ = 3.33 – 8.09) and flat heavy REE distribution patterns with variable Eu anomalies (Eu/Eu* = 0.74 – 1.23).

6.3. Zircon trace element

Trace element compositions of zircon grains separated from the Baogutu intrusions are listed in Table 2 and illustrated on Fig. 6. The

Table 1
Compositions of major oxides (in wt%) and trace elements (in ppm) of the Baogutu intrusions.

Sample	Ab13-17b	Ab13-19b	Ab13-21b	Ab13-23b	07HT112	07HT113	07HT95	07HT96	07HT94	07HT97	ZK02-1	ZK02-3	ZK02-9
Intrusion	I	I	I	I	I	I	II	II	II	II	III	III	III
SiO_2	54.69	51.69	60.13	57.74	57.51	62.33	66.28	66.49	59.39	65.95	57.93	58.38	61.68
TiO_2	0.81	0.90	0.65	0.87	0.76	0.39	0.53	0.52	0.39	0.36	0.48	0.48	0.42
Al_2O_3	16.30	19.60	17.24	17.06	17.43	16.41	15.49	15.39	15.44	14.97	16.69	16.09	15.56
ΣFe_2O_3	7.71	8.17	5.70	6.97	6.86	5.53	4.39	4.22	5.70	4.85	7.36	7.33	5.60
FeO	5.83	5.71	2.91	3.90	N.A.	N.A.	N.A.	N.A.	N.A.	N.A.	N.A.	N.A.	N.A.
MnO	0.12	0.13	0.09	0.11	0.11	0.08	0.05	0.06	0.07	0.03	0.10	0.09	0.07
MgO	5.89	4.85	3.23	4.08	4.46	2.74	2.10	2.16	2.82	1.84	3.73	3.75	2.36
CaO	7.23	8.23	5.68	5.94	6.31	4.98	3.86	3.72	3.98	2.98	5.97	5.13	3.97
Na_2O	3.62	4.30	4.26	4.28	3.69	4.99	3.85	3.91	4.48	4.43	4.40	4.23	5.29
K_2O	1.34	0.43	1.28	1.12	1.27	1.10	2.26	2.45	2.16	2.70	1.40	1.42	1.31
P_2O_5	0.15	0.21	0.15	0.20	0.15	0.15	0.11	0.10	0.11	0.11	0.15	0.15	0.13
LOI	1.95	1.13	1.39	1.77	1.10	1.14	1.01	1.01	5.30	1.48	1.62	2.78	3.46
Total	98.04	98.69	98.56	98.53	98.55	99.85	98.92	99.00	99.85	99.70	99.84	99.84	99.84
$Mg^{\#}$	0.45	0.40	0.42	0.42	0.57	0.50	0.49	0.51	0.50	0.43	0.50	0.51	0.46
Fe^{3+}/Fe^{2+}	0.27	0.14	0.24	0.30									
Cs	0.80	0.43	0.53	0.93	1.11	0.60	1.34	1.34	1.33	1.48	1.29	1.30	2.08
Rb	21.00	5.20	23.00	19.30	22.96	13.57	46.63	41.09	46.32	65.57	31.00	31.20	26.80
Ba	414	275	500	504	731	603	772	769	805	799	440	596	606
Th	0.96	0.33	1.72	1.10	1.45	1.71	4.96	5.44	4.65	6.12	1.00	2.14	3.24
U	0.33	0.16	0.49	0.38	0.43	0.45	1.10	1.23	1.98	1.94	0.39	0.56	1.08
Nb	1.30	1.50	2.10	2.90	1.91	2.47	4.08	3.90	3.61	3.96	1.77	1.93	2.32
Ta	0.20	0.20	0.20	0.30	0.30	0.23	0.35	0.38	0.35	0.35	0.19	0.17	0.21
La	6.40	7.40	9.90	11.20	7.80	10.80	13.62	14.97	12.52	9.43	8.58	8.16	10.22
Ce	14.10	17.50	21.30	25.70	16.91	22.42	27.76	29.77	26.83	19.01	19.84	19.10	22.80
Pr	2.01	2.47	2.74	3.42	2.54	3.20	3.61	3.83	3.65	2.63	2.82	2.54	3.16
Sr	765	1060	757	724	878	680	425	421	526	415	494	518	476
Nd	8.70	10.90	11.60	13.90	11.75	13.55	14.90	14.74	15.22	11.04	11.68	10.92	13.20
Zr	55	34	98	121	64	124	177	166	152	179	95	115	149
Hf	1.60	1.20	2.70	3.00	1.90	3.04	4.32	4.38	3.89	4.60	2.01	2.53	3.33
Sm	2.41	2.45	2.78	3.65	2.84	2.91	3.08	2.89	3.29	2.36	2.72	2.56	2.94
Eu	0.74	0.87	0.82	1.09	0.98	0.90	0.81	0.82	0.92	0.76	0.87	0.81	0.86
Gd	2.37	2.27	2.53	3.68	2.92	2.77	3.15	2.65	3.16	2.39	2.56	2.40	2.66
Tb	0.33	0.29	0.35	0.54	0.39	0.40	0.40	0.39	0.45	0.33	0.44	0.40	0.43
Dy	2.10	1.85	2.29	3.26	2.46	2.36	2.66	2.45	2.94	2.03	2.76	2.66	2.84
Y	10.90	9.80	11.80	17.40	13.83	13.55	15.38	14.70	16.16	12.50	14.72	13.66	15.72
Ho	0.43	0.36	0.45	0.66	0.50	0.49	0.54	0.49	0.59	0.45	0.54	0.54	0.57
Er	1.28	1.08	1.31	1.87	1.41	1.39	1.58	1.50	1.71	1.28	1.58	1.62	1.70
Tm	0.22	0.20	0.24	0.29	0.21	0.22	0.25	0.21	0.25	0.20	0.23	0.25	0.28
Yb	1.11	1.05	1.34	1.86	1.45	1.42	1.67	1.66	1.73	1.37	1.59	1.58	1.71
Lu	0.18	0.16	0.17	0.26	0.20	0.21	0.26	0.25	0.26	0.23	0.28	0.26	0.30
REE	42.38	48.85	57.82	71.38	52.36	63.04	74.29	76.62	73.52	53.51	56.49	53.80	63.67
$(La/Yb)_N$	4.14	5.06	5.30	4.32	3.86	5.46	5.85	6.47	5.19	4.94	3.87	3.70	4.29
Eu/Eu*	0.95	1.13	0.95	0.91	1.04	0.97	0.80	0.91	0.87	0.98	1.01	1.00	0.94

Sample	ZK02-12	ZK02-16	ZK02-20	ZK02-23	ZK02-27	ZK02-31	ZK02-34	ZK02-44	ZK02-46	ZK02-49	ZK02-51	Ab13-47b	Ab13-48b
Intrusion	III	III	III	III	III	III	III	III	III	III	III	VI	VI
SiO_2	62.05	60.94	63.98	62.97	61.96	62.47	62.65	62.65	63.21	63.56	63.36	56.95	58.07
TiO_2	0.41	0.41	0.40	0.44	0.37	0.40	0.36	0.39	0.42	0.40	0.38	0.69	0.72
Al_2O_3	16.06	15.29	15.35	15.12	15.29	16.04	14.57	16.13	14.77	15.19	16.02	16.56	17.08
ΣFe_2O_3	5.92	5.51	5.79	6.20	5.12	5.90	4.80	3.59	5.07	5.68	5.38	6.25	6.58
FeO	N.A.	N.A.	N.A.	N.A.	N.A.	N.A.	N.A.	N.A.	N.A.	N.A.	N.A.	4.97	4.92
MnO	0.08	0.07	0.08	0.08	0.07	0.06	0.07	0.07	0.07	0.05	0.07	0.11	0.09
MgO	2.68	2.18	2.29	2.29	2.47	1.80	1.69	1.11	1.49	1.91	2.29	5.33	3.25
CaO	4.07	4.80	4.20	4.53	3.98	3.99	5.73	5.21	4.61	3.03	4.25	5.96	5.71
Na_2O	4.72	4.50	4.49	4.50	3.86	4.09	3.37	0.63	2.11	4.30	4.53	4.15	3.81
K_2O	1.84	1.49	2.26	2.14	2.37	2.19	2.00	3.25	1.98	2.00	2.11	1.42	1.37
P_2O_5	0.13	0.14	0.13	0.14	0.10	0.13	0.11	0.14	0.11	0.13	0.13	0.13	0.17
LOI	1.86	4.52	0.85	1.39	4.23	2.78	4.53	6.73	6.04	3.59	1.35	2.19	1.41
Total	99.82	99.85	99.82	99.80	99.84	99.86	99.86	99.90	99.89	99.84	99.85	97.71	97.05
$Mg^{\#}$	0.48	0.44	0.44	0.42	0.49	0.38	0.41	0.38	0.37	0.40	0.46	0.47	0.35
Fe^{3+}/Fe^{2+}												0.37	0.25
Cs	1.44	2.22	1.74	1.34	1.81	3.06	3.58	6.82	5.70	0.79	1.75	1.98	1.50
Rb	33.60	33.60	40.80	42.20	41.80	45.20	43.00	70.20	45.40	16.14	45.00	25.30	32.00
Ba	722	518	748	642	776	640	446	430	338	354	630	430	458
Th	5.44	3.00	2.80	3.22	4.46	3.36	2.62	3.62	2.26	1.91	3.20	0.88	1.84
U	1.60	0.90	1.04	1.07	1.39	1.14	0.86	1.03	0.74	0.49	0.68	0.35	1.63
Nb	2.36	2.26	2.38	2.58	2.68	2.58	1.98	2.30	2.26	1.70	2.16	1.60	2.10
Ta	0.27	0.23	0.20	0.22	0.37	0.28	0.14	0.24	0.17	0.17	0.19	0.10	0.20
La	12.24	11.50	12.62	11.46	10.72	11.44	9.90	11.64	10.02	9.78	10.44	5.90	8.40
Ce	26.80	25.80	28.40	26.40	24.20	26.00	22.60	25.40	23.80	22.60	24.20	13.20	18.50
Pr	3.44	3.40	3.66	3.50	3.10	3.36	3.08	3.48	3.08	3.10	3.20	1.81	2.50
Sr	520	460	448	480	460	416	368	197	230	762	456	627	558

(*continued on next page*)

Table 1 (*continued*)

Sample	ZK02-12	ZK02-16	ZK02-20	ZK02-23	ZK02-27	ZK02-31	ZK02-34	ZK02-44	ZK02-46	ZK02-49	ZK02-51	Ab13-47b	Ab13-48b
Nd	14.14	14.16	15.20	14.38	12.74	14.08	12.58	13.62	13.10	13.74	13.26	7.90	10.40
Zr	164	144	176	146	144	151	130	152	136	61	130	66	84
Hf	3.64	3.16	3.83	3.25	3.21	3.23	2.68	3.18	2.77	1.36	2.65	1.80	2.50
Sm	3.02	3.08	3.08	2.94	2.54	3.14	2.74	2.62	2.92	2.60	2.76	2.03	2.67
Eu	0.87	0.78	0.83	0.83	0.70	0.82	0.70	0.68	0.88	1.05	0.73	0.66	0.76
Gd	2.78	2.74	3.18	2.72	2.56	2.80	2.50	2.28	2.82	2.60	2.56	1.99	2.51
Tb	0.45	0.46	0.51	0.43	0.44	0.43	0.42	0.38	0.47	0.42	0.41	0.29	0.34
Dy	2.80	3.06	3.10	2.90	2.84	2.80	2.56	2.54	2.96	2.40	2.60	1.83	2.20
Y	15.90	16.50	17.52	16.82	15.80	16.26	14.54	13.90	16.22	12.22	15.32	9.20	11.30
Ho	0.58	0.60	0.62	0.58	0.58	0.60	0.50	0.47	0.59	0.45	0.54	0.34	0.43
Er	1.74	1.74	1.92	1.68	1.73	1.69	1.50	1.51	1.71	1.27	1.57	1.06	1.36
Tm	0.27	0.26	0.26	0.28	0.28	0.28	0.22	0.22	0.26	0.19	0.24	0.17	0.21
Yb	1.71	1.79	1.90	1.75	1.81	1.87	1.53	1.50	1.67	1.31	1.68	0.95	1.34
Lu	0.32	0.32	0.35	0.32	0.30	0.30	0.27	0.27	0.28	0.20	0.26	0.15	0.21
REE	71.16	69.69	75.63	70.17	64.54	69.61	61.10	66.61	64.56	61.71	64.45	38.28	51.83
$(La/Yb)_N$	5.13	4.61	4.76	4.70	4.25	4.39	4.64	5.57	4.30	5.36	4.46	4.45	4.50
Eu/Eu*	0.92	0.82	0.81	0.90	0.84	0.85	0.82	0.85	0.94	1.23	0.84	1.00	0.90

Sample	Ab13-50b	Ab13-51b	Ab13-52b	Wb13-3	Wb13-7	Wb13-8	09BGT-55	ZK102-G18	ZK203-3	ZK203-5	ZK601-3
Intrusion	VI	VI	VI	V	V	V	V	V	V	V	V
SiO_2	58.03	56.7	63.59	66.51	65.95	62.87	66.07	61.34	57.08	59.22	62.11
TiO_2	0.80	0.71	0.57	0.61	0.58	0.69	0.45	0.49	0.52	0.48	0.46
Al_2O_3	17.36	16.64	15.94	14.92	15.57	16.68	14.99	15.37	17.19	17.14	16.4
ΣFe_2O_3	6.89	6.49	4.99	4.33	3.6	1.87	3.79	4.34	7.3	5.01	5.24
FeO	4.79	5.10	3.65	1.70	2.50	1.33	N.A.	N.A.	N.A.	N.A.	N.A.
MnO	0.11	0.12	0.07	0.02	0.02	0.04	0.02	0.03	0.07	0.05	0.03
MgO	3.94	5.39	2.48	2.33	2.39	4.18	2.17	2.73	3.86	3.63	3.23
CaO	6.79	5.99	4.65	2.48	3.49	6.86	3.95	2.77	5.81	5.89	4.75
Na_2O	4.04	4.31	3.77	3.98	4.16	5.06	5.66	6.73	4.72	5.41	4.87
K_2O	1.15	1.05	2.28	2.67	1.64	0.62	1.49	2.46	1.50	1.39	1.13
P_2O_5	0.19	0.14	0.13	0.14	0.14	0.16	0.13	0.18	0.18	0.17	0.14
LOI	0.86	2.19	1.49	1.88	1.59	1.39	0.94	2.70	1.43	1.26	1.48
Total	99.47	97.71	98.63	98.32	98.78	99.13	99.66	99.12	99.65	99.63	99.85
$Mg^{\#}$	0.39	0.47	0.35	0.43	0.43	0.71	0.53	0.56	0.51	0.59	0.55
Fe^{3+}/Fe^{2+}	0.13	0.37	0.32	0.76	0.46	0.20					
Cs	0.98	2.06	0.84	1.97	3.24	2.87	1.57	2.88	4.18	2.68	1.54
Rb	22.9	21.1	40.6	96.8	90.0	34.9	72.8	114.2	74.2	62.4	41.2
Ba	533	412	685	853	484	205	452	314	380	462	272
Th	1.51	0.94	2.54	4.55	4.71	2.7	4.8	4.32	3.24	2.36	4.46
U	0.58	0.37	0.62	1.93	1.65	0.68	1.75	1.26	1.04	0.85	1.37
Nb	2.50	1.60	2.20	4.00	4.20	3.10	3.72	3.06	2.36	2.26	3.18
Ta	0.20	0.20	0.20	0.40	0.40	0.30	0.28	0.31	0.31	0.17	0.27
La	9.50	6.50	9.60	12.00	15.80	8.20	14.80	7.62	8.66	10.76	19.96
Ce	21.50	14.80	21.00	26.40	33.40	20.70	33.20	22.40	20.60	24.20	42.40
Pr	2.98	2.05	2.83	3.41	4.13	3.19	4.22	3.34	2.86	3.16	5.10
Sr	694	697	557	399	577	651	498	438	756	588	590
Nd	12.30	9.00	11.20	13.80	15.20	14.00	17.12	14.34	12.10	12.94	20.00
Zr	88	69	112	151	161	118	175	138	117	104	168
Hf	2.40	2.00	3.20	4.10	4.20	3.10	3.70	2.75	2.29	2.28	3.11
Sm	3.10	2.24	2.80	3.40	3.46	3.60	3.78	3.50	2.88	2.64	3.66
Eu	0.96	0.77	0.68	0.80	0.82	0.97	0.88	0.85	0.93	0.89	0.99
Gd	3.08	2.54	2.58	3.16	3.33	3.52	3.32	2.98	2.36	2.52	3.12
Tb	0.46	0.32	0.36	0.45	0.47	0.52	0.53	0.49	0.41	0.36	0.50
Dy	2.64	2.01	2.37	2.84	3.04	2.95	3.44	3.14	2.58	2.36	3.02
Y	14.20	10.8	12.8	15.5	16.5	16.4	18.62	15.82	12.94	13.18	16.98
Ho	0.54	0.41	0.48	0.57	0.61	0.63	0.69	0.59	0.51	0.44	0.61
Er	1.72	1.19	1.48	1.77	1.77	1.73	1.93	1.64	1.32	1.35	1.78
Tm	0.23	0.19	0.25	0.26	0.31	0.31	0.30	0.26	0.21	0.20	0.26
Yb	1.53	1.18	1.49	1.79	1.91	1.72	2.12	1.64	1.43	1.35	1.77
Lu	0.22	0.19	0.23	0.27	0.26	0.27	0.35	0.27	0.24	0.24	0.28
REE	60.76	43.39	57.35	70.92	84.51	62.31	86.68	63.06	57.09	63.41	103.45
$(La/Yb)_N$	4.45	3.95	4.62	4.81	5.93	3.42	5.01	3.33	4.34	5.72	8.09
Eu/Eu*	0.95	0.99	0.77	0.75	0.74	0.83	0.76	0.80	1.09	1.05	0.90

$Mg^{\#} = Mg/(Mg + Fe)$.
N.A. = not applied.
$Eu/Eu^* = Eu_N/(Sm_N \times Gd_N)^{1/2}$.

total REE abundances vary from 347 ppm to 2565 ppm. Chondrite-normalized REE patterns are characterized by a steep increase from La_N to Lu_N with strongly positive Ce anomalies and weakly negative Eu anomalies, which are typical characteristics of magmatic zircons.

7. Estimates of magmatic oxidation state

7.1. Estimates of magmatic oxidation state based on amphibole compositions

Amphibole is widely developed in igneous rocks. The stability of

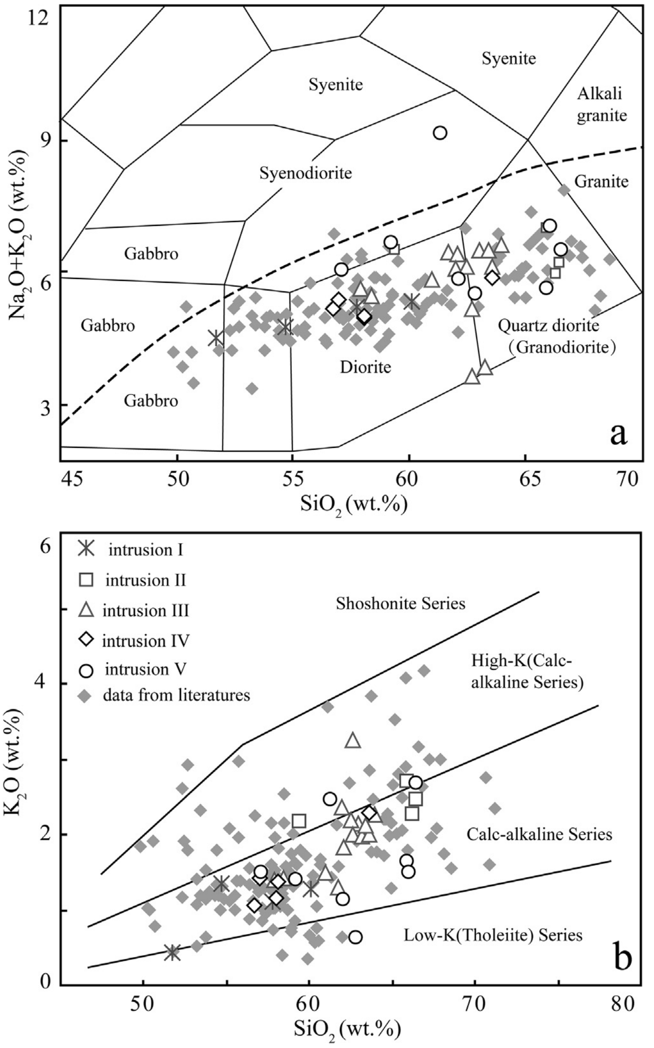

Fig. 4. Classification diagrams of the Baogutu intrusions (literature data from: Zhang et al., 2006b; Shen et al., 2009; Tang et al., 2010; Shen and Pan, 2013; Wei and Zhu, 2015; Cao et al., 2016). (a) Total alkali vs. silica (after Middlemost, 1994). The alkaline and subalkaline division is after Irvine and Baragar (1971). (b) Potassium vs. silica (Rickwood, 1989).

amphibole depends on oxidation state, H_2O content and melt composition (Schmidt, 1992; Sisson and Grove, 1993; Grove et al., 2003). Experiments, combined with oxygen fugacity–amphibole composition regression analyses, show that oxygen fugacity is closely correlated with Mg* of amphibole (Scaillet and Evans, 1999; Ridolfi et al., 2008, 2010):

$$\Delta NNO = 1.644Mg - 4.01(R^2 = 0.89)$$

where Mg* = Mg + Si/47 - $^{VI}Al/9–1.3^{VI}Ti + Fe^{3+}/3.7 + Fe^{2+}/5.2 - {}^{B}Ca/20 - {}^{A}Na/2.8 + {}^{A}[]/9.5$. This formulation is estimated to be accurate within 0.22 log fO_2 units (1σ; Ridolfi et al., 2010), and is in agreement with the uncertainty expected from experiments (0.2 – 0.3 logfO_2 units; Scaillet and Evans, 1999; Pichavant et al., 2002). This oxygen barometer is valid for magmas in the range of 550–1120 °C, < 1200 MPa, and ΔNNO − 1 to ΔNNO + 5. This amphibole Mg* oxygen-barometer was initially applied to subduction-related volcanic rocks and widely used on intermediate igneous rocks. Its reliability is tested recently. For example, the logfO_2 values based on amphibole compositions from the Wandongshan monzogranite porphyry related with the Beiya Au deposit of southwest China range from ΔNNO + 1.0 to ΔNNO + 1.9, which are slightly higher than those of the Bailiancun monzogranite porphyry (ΔNNO + 0.4 to ΔNNO + 0.7). These logfO_2 values are consistent with the values based on zircon compositions (Bao et al., 2018). The logfO_2 values (ΔNNO + 0.3 to ΔNNO + 1.5) based on amphibole compositions in the Baguio diorite porphyry from northern Luzon of Philippines are similar to the values estimated from co-existing Fe–Ti oxides (Cao et al., 2018). It should be noted that the amphibole analyzed should have early–stage textures and show homogeneous compositions, because late–stage amphiboles may overestimate the original magmatic oxidation state.

Amphibole in the Baogutu intrusions is calcic and is classified as magnesiohornblende (Fig. 3b). The crystallization pressures, temperatures and logfO_2 values were estimated based on amphibole compositions (Supplementary Table 1B, Fig. 7). Amphibole in the intrusion I yields pressures of 0.72 – 3.03 kbar, temperatures of 790 – 846 °C, and logfO_2 values varying from △FMQ + 1.7 to ΔFMQ + 3.0. Amphibole in the intrusion II gives similar pressures (0.32 – 2.93 kbar), temperatures (793 – 837 °C), and logfO_2 values (ΔFMQ + 2.1 to ΔFMQ + 3.5). Amphibole in the intrusion III produces lower pressures (0.14 – 1.34 kbar), temperatures (748 – 772 °C), and similar logfO_2 values (ΔFMQ + 1.9 to ΔFMQ + 2.7). The pressures, temperatures and logfO_2 values estimated for the intrusion IV are 1.11 – 1.93 kbar, 789 – 848 °C, and ΔFMQ + 2.2 to ΔFMQ + 3.1, respectively. Amphibole in the intrusion V is homogeneous in composition, suggesting pressures of 0.17 – 1.63 kbar, temperatures of 761 – 806 °C, and logfO_2 values varying from ΔFMQ + 2.1 to ΔFMQ + 3.4. The average logfO_2 value is ΔFMQ + 2.5 (Fig. 7a–b). The correlation between logfO_2 values and temperatures is not obvious (Fig. 7c), while logfO_2 values increase from △FMQ + 1.7 to ΔFMQ + 3.5 with decrease pressures (Fig. 7d).

7.2. Estimates of magmatic oxidation state with magnetite–ilmenite oxygen-barometer

The magnetite–ilmenite oxygen barometer is widely used to estimate magmatic oxygen fugacity with the assumed equilibrium between these two Fe–Ti oxides (Andersen and Lindsley, 1985; Ghiorso and Sack, 1991; Audétat and Pettke, 2006; Ghiorso and Evans, 2008; Sauerzapf et al., 2008). However, these minerals are prone to re-equilibrate in slowly cooled plutonic rocks or in hydrothermal rocks (Venezky and Rutherford, 1999; Idrus et al., 2007; Anderson et al., 2008). Consequently, coexisting magnetite and ilmenite may not be in equilibrium. In the Baogutu intrusions, primary magnetite and ilmenite mainly occur as interstitial crystals and inclusions. We analyzed ilmenite and magnetite where textural equilibrium can be demonstrated. We used the ILMAT spreadsheet (Lepage, 2003) to calculate temperatures and logfO_2 values from the coexisting magnetite-ilmenite pair.

Magnetite and ilmenite are common in the Baogutu intrusion I. However, ilmenite grains are partly altered to sphene and rutile, or postdate magnetite. Consequently, no reliable data were obtained from magnetite–ilmenite pair for the intrusion I. In the intrusion II, magnetite is common, whereas ilmenite is subordinate. Although some magnetite grains in the intrusion II were replaced by hematite along crystal lattice, magnetite and ilmenite occurring as intergrowths with straight boundaries and without exsolution textures were investigated for oxygen fugacity calculation (Fig. 8a). Representative magnetite–ilmenite pairs yield logfO_2 values varying from ΔFMQ + 1.6 to ΔFMQ + 3.9 (Fig. 8c). No equilibrated magnetite–ilmenite pairs were found in the intrusions III and IV. Several magnetite– ilmenite pairs occur as inclusions in the intrusion V (Fig. 8b), in which eight representative pairs yield logfO_2 values of ΔFMQ + 1.9 to ΔFMQ + 3.1 (Fig. 8c). The average logfO_2 value for the Baogutu intrusions defined by magnetite–ilmenite pair is ΔFMQ + 2.7 (Fig. 8d), which is in agreement with the logfO_2 values based on amphibole compositions.

7.3. Whole-rock Fe^{3+}/Fe^{2+} ratios

Whole-rock Fe^{3+}/Fe^{2+} ratio is an empirical redox indicator (Brett and Sato, 1984; Rhodes and Vollinger, 2005), which can only be used to

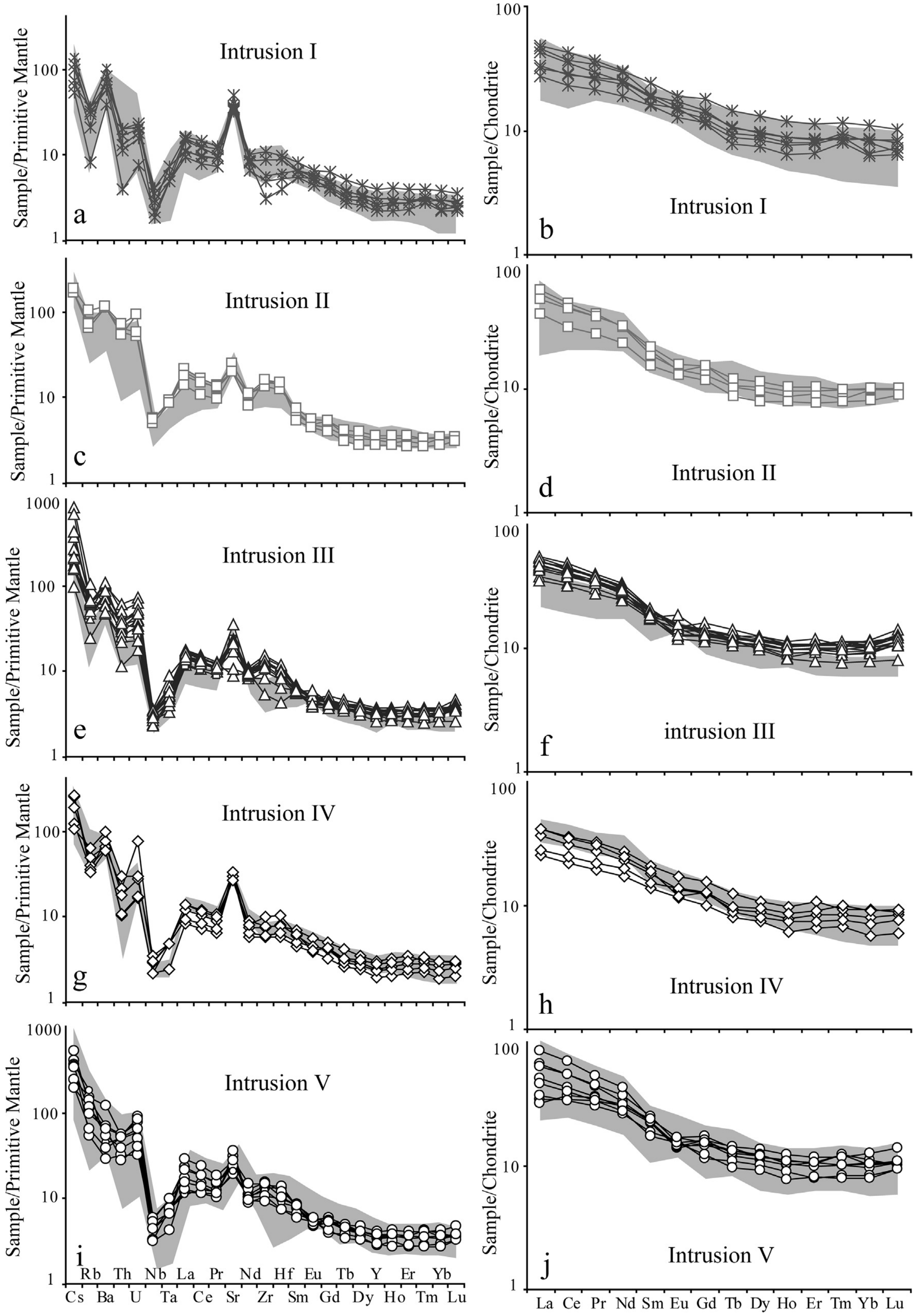

Fig. 5. Primary mantle-normalized multi-elements diagrams and chondrite-normalized REE distribution patterns for the Baogutu intrusions (shaded areas are from: Shen et al., 2009; Tang et al., 2010; Shen and Pan, 2013; Wei and Zhu, 2015; Cao et al., 2016). Normalization values are from Sun and McDonough (1989).

fresh igneous rocks. Sufficiently fresh samples were selected for this method based on detailed microscopic observations. These samples have low loss on ignition (LOI, < 2.0 wt%), and their Fe_2O_3/FeO ratios do not correlate with LOI values.

The Fe^{3+}/Fe^{2+} ratios for the intrusion I range from 0.42 to 1.68, which belong to magnetite series (Fig. 9a) and correspond to

Table 2
Concentrations of trace elements in zircons from the Baogutu intrusions (in ppm, by LA-ICP-MS).

Analysis number	Intrusion	P	Ti	Y	Nb	La	Ce	Pr	Nd	Sm	Eu	Gd	Tb
Ab13-23b-1	I	228	9.18	1320	0.40	0.01	7.45	0.13	2.38	5.99	1.60	31.68	10.94
Ab13-23b-2	I	227	8.45	902	0.31	0.26	5.26	0.16	2.08	3.47	1.05	17.42	6.25
Ab13-23b-4	I	212	9.45	931	0.30	0.02	4.75	0.08	1.60	3.32	1.03	17.54	6.43
Ab13-23b-5	I	160	23.13	720	0.36	0.41	5.37	0.13	1.44	2.42	0.82	13.52	4.93
Ab13-23b-6	I	160	146.53	788	0.34	0.05	4.55	0.08	1.46	2.83	0.87	14.93	5.45
Ab13-23b-7	I	203	30.26	1081	0.31	0.30	8.95	0.18	2.23	4.62	1.33	22.92	7.94
Ab13-23b-8	I	224	12.35	1062	0.38	0.02	4.99	0.09	1.76	3.79	1.18	21.07	7.55
Ab13-23b-10	I	163	14.52	713	0.28	0.12	4.42	0.08	1.19	2.33	0.80	12.32	4.58
Ab13-23b-11	I	184	7.21	802	0.30	0.02	4.90	0.09	1.32	2.76	0.91	14.73	5.40
Ab13-23b-14	I	205	10.19	1044	0.32	0.01	5.12	0.12	2.07	3.98	1.33	21.18	7.63
15BGT-1–1	II	270	10.23	1507	0.49	0.02	9.69	0.19	3.06	5.79	1.59	32.01	11.16
15BGT-1–2	II	150	3.11	484	0.59	0.25	7.51	0.08	0.62	1.03	0.32	6.18	2.48
15BGT-1–4	II	221	3.80	844	0.76	0.51	11.75	0.20	1.68	2.50	0.74	12.68	4.79
15BGT-1–5	II	214	11.02	1079	0.46	0.02	7.47	0.13	2.47	4.42	1.24	21.36	7.57
15BGT-1–10	II	205	2.99	623	0.85	0.63	10.25	0.18	1.19	1.36	0.38	7.65	3.09
15BGT-1–11	II	166	3.30	665	0.97	0.15	10.25	0.07	0.71	1.37	0.46	8.35	3.32
15BGT-1–12	II	169	6.00	538	0.46	0.01	5.27	0.04	0.52	1.47	0.49	7.86	3.13
15BGT-1–13	II	172	4.12	797	0.60	0.01	7.51	0.07	1.49	2.75	0.70	13.94	5.12
15BGT-1–14	II	148	2.65	526	0.65	0.16	9.28	0.06	0.76	1.24	0.33	7.07	2.73
15BGT-1–15	II	281	5.86	1003	0.54	0.84	9.78	0.42	3.91	4.64	1.19	21.16	7.32
09BGT-18–1	III	167	8.35	598	0.39	bdl	6.16	0.03	0.62	1.54	0.54	7.70	2.97
09BGT-18–3	III	255	8.36	857	0.53	bdl	8.07	0.04	0.86	2.21	0.68	12.62	4.81
09BGT-18–4	III	242	10.43	1018	0.48	bdl	8.16	0.07	1.43	3.06	0.93	17.45	6.50
09BGT-18–5	III	207	9.58	801	0.43	bdl	8.20	0.05	0.93	1.94	0.69	9.76	3.84
09BGT-18–6	III	199	9.03	769	0.41	0.01	7.68	0.05	1.17	2.04	0.84	10.51	3.87
09BGT-18–8	III	236	10.69	757	0.45	bdl	7.84	0.04	0.91	2.17	0.57	12.54	4.69
09BGT-18–9	III	138	20.25	381	0.35	0.10	4.84	0.06	0.49	1.00	0.39	4.99	1.84
09BGT-18–10	III	173	8.03	631	0.34	bdl	5.57	0.04	0.89	1.81	0.65	9.30	3.48
09BGT-18–14	III	204	10.50	751	0.50	0.01	7.30	0.03	0.89	1.71	0.71	9.46	3.66
Ab13-48b-3	IV	406	10.20	2982	0.97	0.03	19.80	0.27	5.15	10.00	2.15	58.41	21.40
Ab13-48b-4	IV	406	10.55	3247	0.93	0.04	21.71	0.31	5.67	11.06	2.52	68.28	24.38
Ab13-48b-5	IV	303	10.54	1580	0.60	0.02	11.32	0.14	2.56	5.52	1.22	29.94	11.13
Ab13-48b-6	IV	362	20.63	1874	0.62	0.03	12.98	0.19	3.26	6.55	1.47	38.19	13.41
Ab13-48b-7	IV	225	8.77	1603	0.41	0.01	10.22	0.14	3.41	6.94	1.46	36.71	12.68
Ab13-48b-8	IV	331	7.40	1974	0.53	0.02	13.49	0.20	3.58	7.46	1.41	40.13	14.66
Ab13-48b-9	IV	585	15.02	3844	1.95	0.02	37.79	0.27	5.29	11.73	2.74	79.48	29.32
Ab13-48b-10	IV	321	6.89	1801	0.51	bdl	12.00	0.16	3.47	6.16	1.36	35.26	12.88
Ab13-48b-11	IV	245	8.59	1079	0.32	0.07	7.54	0.10	1.87	4.22	0.93	22.93	8.11
Ab13-48b-12	IV	387	11.28	1729	0.70	0.03	13.00	0.15	2.74	6.13	1.38	33.65	12.08
Ab13-48b-13	IV	334	9.46	2087	0.55	0.07	13.30	0.21	3.80	7.89	1.60	43.86	15.69
Ab13-48b-14	IV	518	13.10	3698	1.93	0.02	35.96	0.30	5.45	11.56	2.49	72.06	26.87
Ab13-48b-15	IV	355	9.88	2684	0.81	0.02	19.47	0.27	4.87	10.13	2.13	58.09	20.86
Wb13-3–1	V	184	16.90	594	0.68	0.18	8.35	0.29	2.63	1.99	0.66	7.97	3.05
Wb13-3–2	V	135	28.59	465	0.50	0.03	6.40	0.06	0.65	1.27	0.53	6.70	2.56
Wb13-3–3	V	179	44.76	661	0.70	0.03	7.67	0.06	0.94	1.75	0.70	9.11	3.51
Wb13-3–4	V	166	23.81	459	0.42	0.06	7.40	0.08	0.96	1.71	0.63	8.85	3.04
Wb13-3–6	V	212	7.10	795	0.80	0.10	8.30	0.07	1.07	2.12	0.65	11.56	4.77
Wb13-3–8	V	200	6.37	804	0.64	bdl	9.65	0.07	1.20	2.46	0.91	12.82	4.88
Wb13-3–10	V	213	6.27	950	0.75	0.02	11.16	0.10	1.70	3.52	1.45	17.44	6.13
Wb13-3–11	V	185	4.44	591	0.79	0.07	7.53	0.10	0.75	1.56	0.65	8.15	3.13
Wb13-3–12	V	245	8.19	879	0.83	0.37	10.9	0.17	2.10	3.74	0.98	17.00	5.83
Wb13-3–13	V	152	7.45	410	0.57	0.12	5.51	0.09	0.65	1.21	0.42	6.49	2.38
Wb13-3–14	V	174	7.90	637	0.57	0.02	7.29	0.08	0.99	2.06	0.69	9.74	3.58
Wb13-3–15	V	193	6.44	987	0.78	0.12	8.60	0.23	2.83	3.76	0.97	17.92	6.41

Analysis No	Intrusion	Dy	Ho	Er	Tm	Yb	Lu	Hf	Ta	Th	U	REE	Eu/Eu*	Ce^{4+}/Ce^{3+}	T(°C)
Ab13-23b-1	I	124.06	44.63	190	38.26	361	66.53	7589	0.13	66.48	70.85	885	0.36	28.75	765
Ab13-23b-2	I	75.23	29.00	135	29.55	303	60.17	7850	0.12	39.91	66.37	668	0.42	22.77	757
Ab13-23b-4	I	79.55	30.50	138	29.70	296	57.32	8042	0.14	36.71	56.87	666	0.41	33.39	768
Ab13-23b-5	I	59.62	23.19	108	23.32	240	47.37	7536	0.12	32.74	54.50	531	0.44	31.79	864
Ab13-23b-6	I	66.34	25.68	118	25.33	258	50.52	8112	0.13	29.30	54.57	574	0.41	35.62	813
Ab13-23b-7	I	95.11	35.46	157	32.98	320	60.20	7752	0.13	46.41	64.18	749	0.40	31.85	896
Ab13-23b-8	I	91.04	34.96	160	33.69	334	63.84	7266	0.14	33.46	56.15	759	0.40	31.05	795
Ab13-23b-10	I	56.99	22.57	106	23.68	247	49.79	7840	0.12	29.90	56.81	532	0.46	38.69	812
Ab13-23b-11	I	65.78	25.44	119	26.03	272	54.30	8359	0.13	45.20	80.93	592	0.44	38.41	742
Ab13-23b-14	I	88.65	33.71	150	31.69	316	58.84	7721	0.10	35.97	53.55	720	0.44	24.30	775
15BGT-1–1	II	134.64	50.33	222	45.14	427	79.46	8012	0.20	79.94	91.08	1022	0.36	28.63	776
15BGT-1–2	II	32.91	14.39	76	18.48	209	45.81	9706	0.25	69.06	162.16	415	0.38	114.36	669
15BGT-1–4	II	61.63	25.47	130	30.65	335	70.85	9940	0.31	117.51	218.61	688	0.40	59.08	686
15BGT-1–5	II	92.03	35.42	161	33.10	323	61.85	7887	0.19	50.38	71.94	752	0.39	29.71	783
15BGT-1–10	II	42.59	18.50	98	24.00	269	58.59	10,010	0.35	103.55	209.79	536	0.36	74.06	666
15BGT-1–11	II	45.82	20.06	106	25.67	291	63.15	10,056	0.36	95.05	206.64	576	0.41	163.30	674
15BGT-1–12	II	39.93	16.74	84	19.80	214	45.99	8573	0.19	30.24	76.14	439	0.44	123.28	725

(*continued on next page*)

Table 2 (*continued*)

Analysis No	Intrusion	Dy	Ho	Er	Tm	Yb	Lu	Hf	Ta	Th	U	REE	Eu/Eu*	Ce^{4+}/Ce^{3+}	T(°C)
15BGT-1–13	II	63.15	25.03	122	27.77	297	61.79	9223	0.22	76.05	143.64	628	0.35	66.44	692
15BGT-1–14	II	36.61	15.81	82	19.65	219	47.14	10,165	0.29	105.27	216.37	441	0.34	149.91	657
15BGT-1–15	II	86.65	32.86	151	32.56	329	65.40	8774	0.19	72.29	118.87	747	0.37	15.91	723
09BGT-18–1	III	39.65	17.75	95	23.51	270	57.92	7770	0.13	27.70	58.68	524	0.48	146.80	756
09BGT-18–3	III	62.37	26.69	133	30.56	323	64.30	8135	0.16	34.43	67.31	670	0.39	130.55	756
09BGT-18–4	III	80.77	33.10	155	34.43	348	66.22	8019	0.16	35.49	65.68	756	0.39	71.99	778
09BGT-18–5	III	53.25	23.95	125	30.51	344	71.91	7914	0.15	40.70	71.86	674	0.49	135.67	769
09BGT-18–6	III	53.06	23.17	119	28.90	317	65.63	7820	0.13	40.03	71.86	633	0.56	102.88	763
09BGT-18–8	III	60.32	24.75	118	26.16	271	52.18	8427	0.17	26.98	55.07	581	0.34	110.92	780
09BGT-18–9	III	25.34	11.45	61	15.50	181	39.22	7830	0.10	19.25	45.41	347	0.54	93.92	848
09BGT-18–10	III	44.74	19.34	100	24.14	268	56.17	7991	0.12	27.13	54.65	534	0.48	87.32	752
09BGT-18–14	III	50.27	22.72	121	29.53	332	70.03	8358	0.17	29.17	63.16	650	0.54	161.93	778
Ab13-48b-3	IV	264.25	101.45	445	89.85	833	151.44	8202	0.32	222.42	215.64	2002	0.27	41.43	775
Ab13-48b-4	IV	293.73	111.32	485	96.82	895	161.09	8076	0.31	232.65	217.72	2177	0.28	39.37	779
Ab13-48b-5	IV	136.68	53.40	240	49.48	475	87.95	8154	0.21	77.68	100.72	1104	0.29	48.77	779
Ab13-48b-6	IV	162.64	62.27	281	57.31	548	102.28	8203	0.21	99.10	123.15	1290	0.28	40.08	851
Ab13-48b-7	IV	147.87	54.84	238	48.07	447	80.84	8562	0.17	70.29	84.76	1087	0.28	33.13	761
Ab13-48b-8	IV	176.81	67.49	301	61.43	586	105.17	9121	0.21	110.37	135.33	1379	0.25	38.86	744
Ab13-48b-9	IV	354.52	132.94	575	112.38	1024	180.70	7449	0.44	458.72	309.86	2547	0.28	79.92	815
Ab13-48b-10	IV	158.37	60.82	274	56.29	543	98.74	8999	0.20	106.38	133.41	1262	0.28	41.30	738
Ab13-48b-11	IV	97.96	36.88	164	33.42	320	58.01	8574	0.14	40.39	59.22	756	0.29	41.46	759
Ab13-48b-12	IV	149.53	57.92	264	54.59	523	96.26	7895	0.20	91.79	113.25	1214	0.30	51.57	786
Ab13-48b-13	IV	193.65	72.67	321	64.50	612	109.43	8578	0.22	117.94	130.49	1459	0.26	35.26	768
Ab13-48b-14	IV	335.76	130.36	578	114.46	1063	188.90	7958	0.50	502.84	346.06	2565	0.26	72.70	801
Ab13-48b-15	IV	252.14	94.18	412	82.25	768	134.99	8389	0.29	200.98	187.91	1859	0.27	39.87	772
Wb13-3–1	V	41.99	17.62	92	22.59	265	50.43	7946	0.22	54.27	103.43	515	0.51	25.87	828
Wb13-3–2	V	34.73	13.91	73	17.49	204	38.64	8519	0.20	44.82	89.72	399	0.56	98.01	889
Wb13-3–3	V	47.73	19.70	99	24.31	278	52.40	8095	0.22	58.81	112.11	546	0.54	96.12	947
Wb13-3–4	V	38.14	14.41	70	16.26	178	31.91	8077	0.24	27.46	50.99	371	0.50	64.99	867
Wb13-3–6	V	60.72	25.23	123	28.35	297	61.38	7988	0.23	70.73	129.45	625	0.40	90.62	741
Wb13-3–8	V	61.18	25.24	123	28.86	310	65.16	8205	0.22	88.47	123.84	646	0.50	99.60	731
Wb13-3–10	V	73.40	29.84	142	32.62	350	72.65	8000	0.24	105.54	139.15	742	0.57	69.98	729
Wb13-3–11	V	42.46	17.78	92	22.59	263	49.51	7950	0.30	54.42	107.52	510	0.56	81.09	699
Wb13-3–12	V	72.14	27.14	130	29.47	318	55.42	7697	0.23	78.57	122.59	673	0.38	41.26	754
Wb13-3–13	V	31.72	12.70	65	15.59	180	33.29	7896	0.21	34.62	84.06	355	0.45	63.42	745
Wb13-3–14	V	47.88	19.30	97	23.28	269	50.10	8009	0.22	55.95	105.12	531	0.47	73.71	751
Wb13-3–15	V	78.53	31.28	149	33.44	349	68.69	7923	0.26	76.80	143.90	751	0.36	25.03	732

Zircon temperature is estimated based on Ferry and Watson (2007)
Zircon Ce^{4+}/Ce^{3+} and Eu/Eu*ratios are calculated based on Ballard et al. (2002)
Bdl = below the detection limit.

"moderately oxidized" to "strongly oxidized" magmas with $\log fO_2$ values higher than the FMQ buffer (Fig. 9b). The Fe^{3+}/Fe^{2+} ratios (0.29 – 0.65) of the intrusion IV are plotted near the boundary of "magnetite series" and "ilmenite series" magmas (Fig. 9a) and correspond to "moderately reduced" to "moderately oxidized" magmas closing to the FMQ buffer (Fig. 9b). Those of the intrusion V (0.59 – 0.98) are near the boundary of "magnetite series" and "ilmenite series" magmas (Fig. 9a). The average Fe^{3+}/Fe^{2+} ratio of the Baogutu intrusions is 0.71, suggesting magmas between the "magnetite series" and "ilmenite series" (Fig. 9a). The corresponding oxidation state is mainly "moderately oxidized", which is higher than the FMQ buffer (Fig. 9a).

7.4. Zircons Ce^{4+}/Ce^{3+} and Eu/Eu^* ratios

Zircon is a common accessory mineral in intermediate to felsic intrusive rocks, and is resistant to hydrothermal alteration and surficial weathering. Therefore, it can retain its primary chemical and isotopic compositions, and provide chemical information related to its parental magma. Among REE, Ce forms Ce^{4+} and Ce^{3+} under terrestrial conditions. Ce^{4+} preferentially partitions into zircon because of its similar charge and ionic size to Zr^{4+}, whereas other light REE including Ce^{3+} are largely excluded. Thus, zircon grains formed in oxidized magmas show positive Ce anomalies on chondrite-normalized REE diagrams. The Ce^{4+}/Ce^{3+} ratios were used to estimate the oxidation state of parental magmas (Ballard et al., 2002; Liang et al., 2006; Muñoz et al., 2012; Wang et al., 2014; Trail et al., 2011; Smythe and Brenan, 2015, 2016; Zhang et al., 2017). The concentration of Ce^{3+} is commonly estimated based on the concentrations of La and Pr with the assumption that the normalized values of La, Ce^{3+}, and Pr plot along a smooth curve. However, the concentrations of La and Pr are very low in zircon. We therefore employed the calculation method proposed by Ballard et al. (2002), where the abundance of Ce^{3+} is determined from the REE concentrations and whole-rock data on the basis of a lattice-strain model for mineral–melt partition of elements (Blundy and Wood, 1994). Zou et al. (2019) introduced a new parameter (δK) to constrain the reliability of this oxygen barometer. They suggested that only zircons with $\delta K < 3$ can provide credible Ce^{4+}/Ce^{3+} values. We checked our samples with this parameter and found out that only 4 of the 54 zircons tested display $\delta K > 3$, which indicates that the calculated Ce^{4+}/Ce^{3+} ratios are quite credible.

The Eu anomaly of zircon is also indicative of the oxidation state of the parental magmas because Eu^{2+} is excluded from zircon relative to Eu^{3+}. Zircon grains formed under relatively reduced conditions show negative Eu anomalies on chondrite- normalized REE diagrams where most of the Eu is present as Eu^{2+}. Zircon with REE patterns lacking negative Eu anomalies formed under relatively oxidized conditions where most of Eu is present as Eu^{3+} (Burnham and Berry, 2012). The Eu anomaly (Eu/Eu*) is calculated based on chondrite-normalized values of Sm, Eu and Gd concentrations ($Eu/Eu^* = Eu_N/(Sm_N \times Gd_N)^{1/2}$. It should be noted that the zircon Eu/Eu^* ratios can be affected by pre- or co-precipitated minerals. For example, plagioclase preferentially incorporates Eu relative to Sm and Gd, which would produce low Eu/Eu^* ratios in zircon. Amphibole and apatite always show negative Eu anomalies in the chondrite-normalized REE diagram. However, the whole-rock compositions with Eu/Eu^* values varying from 0.74 to 1.23 do not show obvious Eu anomalies. This suggests that the effects on

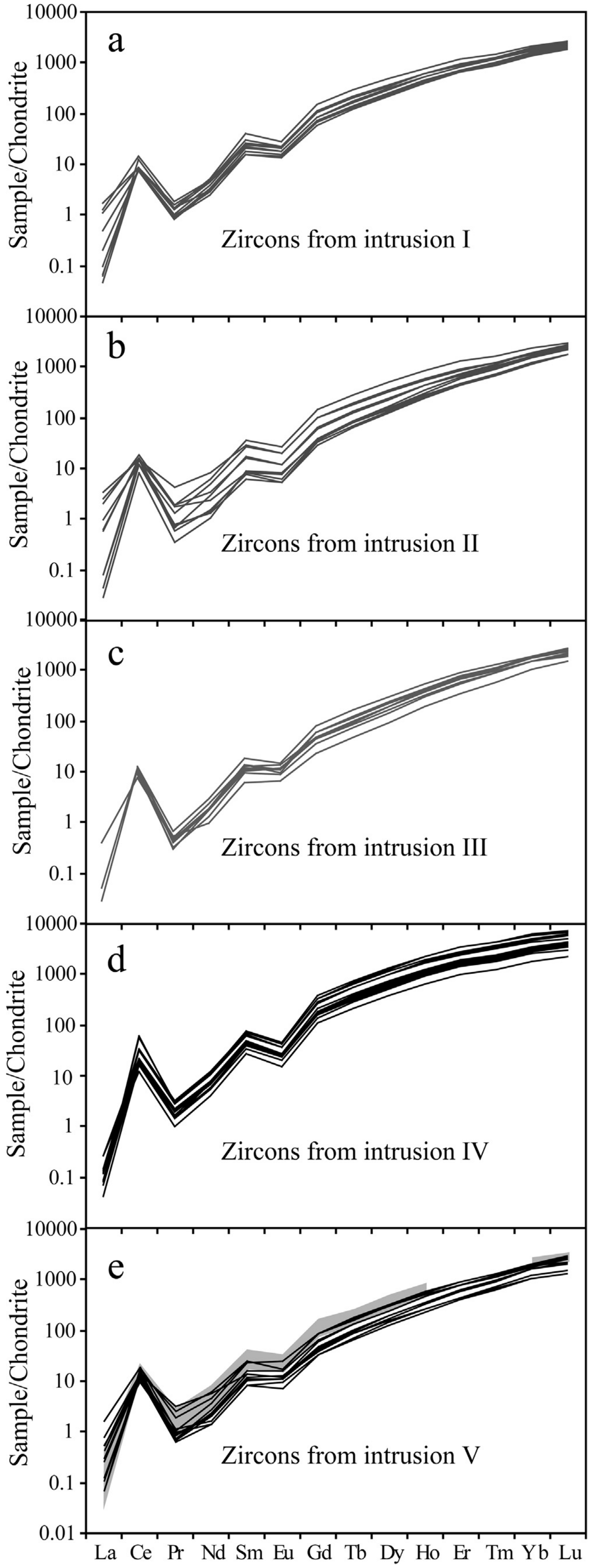

Fig. 6. Chondrite-normalized REE patterns for zircons from the Baogutu intrusions. Normalization values are from Sun and McDonough (1989).

zircon Eu anomalies by pre- or co-precipitated minerals offset each other, and the Eu/Eu* ratios of zircon could also be used to estimate the oxidation state of the Baogutu ore-forming magma.

The calculated Ce^{4+}/Ce^{3+} ratios in zircons from the Baogutu intrusions vary from 15.9 to 163 with Eu/Eu* ratios ranging from 0.25 to 0.57 (Table 2, Fig. 10). Temperatures estimated based on Ti-in-zircon geothermometer of Ferry and Watson (2007) show a large variation from 657 °C to 947 °C (Table 2, Fig. 10). Zircons from the intrusion I display constantly low Ce^{4+}/Ce^{3+} ratios (22.8 – 38.7) and Eu/Eu* ratios (0.36–0.46). Temperatures calculated for these zircons range from 744 °C to 896 °C. Zircons from the intrusion II show variable Ce^{4+}/Ce^{3+} ratios (15.9 – 163) and constantly low Eu/Eu* ratios (0.34 – 0.44). Calculated temperatures range from 657 °C to 783 °C. In comparison, zircons from the intrusion III show pretty higher Ce^{4+}/Ce^{3+} ratios (72.0 – 162), Eu/Eu* ratios (0.34 – 0.56) and temperatures of 752 °C to 848 °C. The Ce^{4+}/Ce^{3+} ratios (33.1 – 79.9) and Eu/Eu* ratios (0.25 – 0.30) for zircons in the intrusion IV are least variable. The temperatures for these zircons range from 738 °C to 851 °C. Zircons from the intrusion V have moderate Ce^{4+}/Ce^{3+} ratios (25.0 – 99.6) and relatively high Eu/Eu* ratios (0.36 – 0.57). Temperatures calculated for these zircons range from 699 °C to 889 °C. There is a positive correlation between the Ce^{4+}/Ce^{3+} and Eu/Eu* ratios (Fig. 10).

8. Discussion

8.1. Oxidation state of the Baogutu ore-forming magma

The magmatic oxidation state of the Baogutu intrusions has been investigated using various mineralogical and geochemical parameters. The oxygen barometer based on amphibole compositions provides logfO_2 values varying from $\triangle$FMQ + 1.7 to ΔFMQ + 3.5 with an average value of ΔFMQ + 2.5, while the magnetite–ilmenite oxygen barometer provides logfO_2 values varying from ΔFMQ + 1.6 to ΔFMQ + 3.9 with an average value of ΔFMQ + 2.7. The whole-rock Fe^{3+}/Fe^{2+} ratios confirm to these logfO_2 estimates ("moderately oxidized"). However, the significance of the zircon Ce^{4+}/Ce^{3+} ratios (15.9 – 163: average 67.0) and Eu/Eu* ratios (0.25 – 0.57: average 0.40) is still inconclusive. Ballard et al. (2002) suggested $Ce^{4+}/Ce^{3+} > 300$ and Eu/Eu$^* > 0.4$ for intrusions with porphyry copper mineralization in northern Chile. Liang et al. (2006) suggested a Ce^{4+}/Ce^{3+} ratio of 120 to divide the ore-bearing and barren porphyries in Yulong, east Tibet. Wang et al. (2014) suggested $Ce^{4+}/Ce^{3+} > 50$ for Miocene ore-forming magmas in the eastern Gangdese belt. Considering these discrepancies, we compared the Ce^{4+}/Ce^{3+} and Eu/Eu* ratios of the Baogutu intrusions with those of typical porphyry copper deposits worldwide (Fig. 11). Seven ore-bearing calc-alkaline intrusions from the Chuquicamata El Abra porphyry copper belt in Chile have extremely high zircon Ce^{4+}/Ce^{3+} ratios (91–2341) and moderate Eu/Eu* ratios (0.23 – 0.95) (Ballard et al., 2002). Zircons from the El Teniente ore deposit have variable Ce^{4+}/Ce^{3+} ratios (26.8 – 2718) and moderate Eu/Eu* ratios (0.17 – 0.64) (Muñoz et al., 2012). Zircons from the Yulong ore-bearing porphyries display variable Ce^{4+}/Ce^{3+} ratios (5–1314) (Liang et al., 2006). Two ore-bearing intrusions from the Lannitang porphyry deposit display high zircon Ce^{4+}/Ce^{3+} ratios (163 – 621) and Eu/Eu* ratios (0.54 – 1.00) (Yu et al., 2016). Four ore-bearing intrusions from the Pulang porphyry copper deposit have moderate to high zircon Ce^{4+}/Ce^{3+} ratios (65 – 1128) and Eu/Eu* ratios (0.5 – 0.7) (Kong et al., 2016). In the eastern Gangdese belt of southern Tibet, magmas associated with several large porphyry Cu–Mo ± Au deposits are characterized by moderate zircon Ce^{4+}/Ce^{3+} ratios (18.6 – 142) and variable Eu/Eu* ratios (0.19 – 0.87) (Wang et al., 2014). Zircons from eight porphyry copper deposits in the central Asian metallogenic domain display moderate to high Ce^{4+}/Ce^{3+} (29 – 592) and Eu/Eu* ratios (0.24 – 0.79, Shen et al., 2015). Our data show that zircons from the Baogutu intrusions have low to moderate Ce^{4+}/Ce^{3+} ratios (15.9 – 163) and Eu/Eu* ratios (0.25 – 0.57, Table 2). These values are

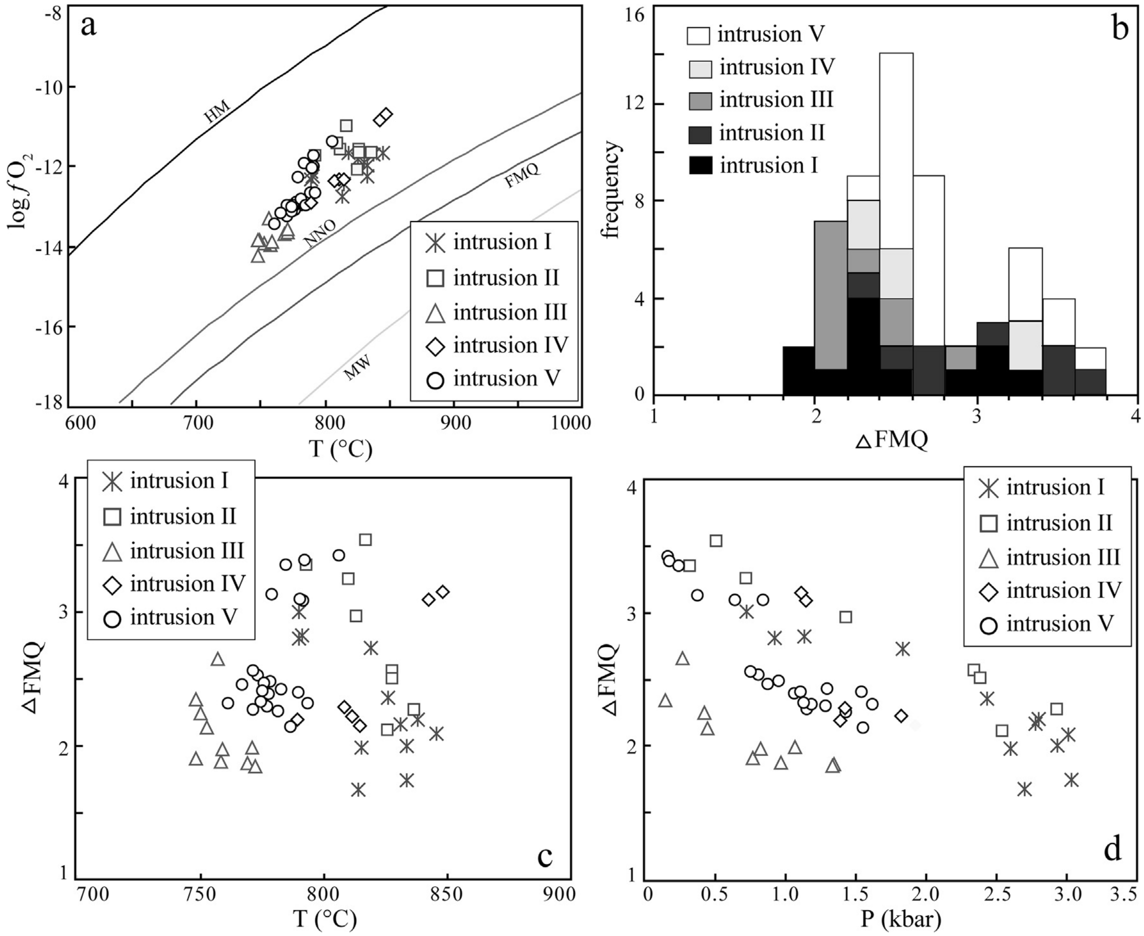

Fig. 7. Plots and histograms of oxidation state, temperature and pressure estimated from amphiboles from the Baogutu intrusions. (a) logfO_2 vs. temperature (at 1kbar pressure). (b) ΔFMQ histogram. (c) ΔFMQ vs. temperature. (d) ΔFMQ vs. pressure. ΔFMQ and temperature were calculated from the spread sheet of Ridolfi et al. (2010); pressure was calculated using equations of Schmidt (1992). HM = hematite–magnetite buffer curve (Spencer and Lindsley, 1981), NNO = nickel–nickel oxide buffer curve (Huebner and Sato, 1970), FMQ = fayalite–magnetite–quartz buffer curve (Huebner, 1971), MW = wustite–magnetite buffer curve (Eugster and Wones, 1962).

obviously lower than those from the circum-pacific metallogenic domain, but in the variation range of porphyry deposits in the Tethyan and central Asian metallogenic domain (Fig. 11).

8.2. Baogutu porphyry copper deposit: Oxidized or reduced?

The Baogutu deposit was considered to be a reduced porphyry copper deposit based on the occurrence of hypogene pyrrhotite and absence of anhydrite and/or hematite (Cao et al., 2014, 2017; Shen and Pan, 2015). Classical porphyry copper deposits are relatively oxidized during magmatic stage in which primary anhydrite is a powerful indicator of the oxidized feature (Sillitoe, 2010). Among thousands of oxidized porphyry copper deposits all over the world, only minorities are reported to contain primary or hydrothermal anhydrite (Hattori and Keith, 2001; Audétat et al., 2004; Liang et al., 2009; Stern et al., 2007; Xiao et al., 2012; Grondahl and Zajaca, 2017), which suggests that anhydrite can not be used solely to constrain the oxidized state of porphyry copper deposits. Moreover, the genesis of hematite in porphyry copper deposits is still controversial. Most of the previously reported hematite grains were considered as secondary phase formed by exsolution (Ballard et al., 2002) or via post-mineralization oxidation (Patricio and Gonzalo, 2001). These happened to be the phenomenon as we observed in the Baogutu intrusions (see Fig. 2g).

Sulfate (SO_4^{2-}) is the dominant sulfur species in magma source with high oxidation state, which facilitates ore-forming metals such as Cu and Au to be released to the magma, and transported to the shallow crust (Botcharnikov et al., 2011; Zajacz et al., 2013). Sulfide crystallization at early stage will consume ore-forming elements in magmas with low oxidation state. Abundant pyrrhotite grains were reported as “inclusions in amphibole” in the Baogutu porphyry (Cao et al., 2014). However, we believe that these “pyrrhotite inclusions” were formed at late hydrothermal stage and could not be magmatic minerals. In fact, the interstitial pyrrhotite grains distributed among plagioclase crystals in the Baogutu porphyry copper deposit (Shen and Pan, 2015) suggest that pyrrhotite crystallized in the late stage of magmatic process. The abundances of magnetite and ilmenite vary among the intrusions (intrusions I and II contain more magnetite, while intrusions III, IV and V contain more ilmenite), which is consistent with the scattered data of Fe^{3+}/Fe^{2+} ratios (Fig. 9). Thus, the Baogutu intrusions locate between the “magnetite series” and “ilmenite series”.

The fO_2 values of the Baogutu ore-forming magma have been discussed by different researchers with multiple methods. Shen and Pan (2013) obtained high logfO_2 values (ΔNNO + 2.7 to ΔNNO + 3.5) for the Baogutu magma based on the empirical formula given by Scaillet and Evans (1999). With the same method, Zhu et al. (2018) identified two magmatic stages for the Baogutu intrusions: the early oxidized stage (logfO_2 = ΔNNO + 2.4) and the late reduced stage (logfO_2 = ΔNNO − 0.6). Shen and Pan (2015) recalculated the redox conditions of the Baogutu primary magma at logfO_2 > NNO + 0 or logfO_2 = ΔFMQ + 1, mainly based on mineral compositions (amphibole, apatite, magnetite–ilmenite), whereas they reported temperatures and fO_2 values for individual magnetite and ilmenite grains instead of

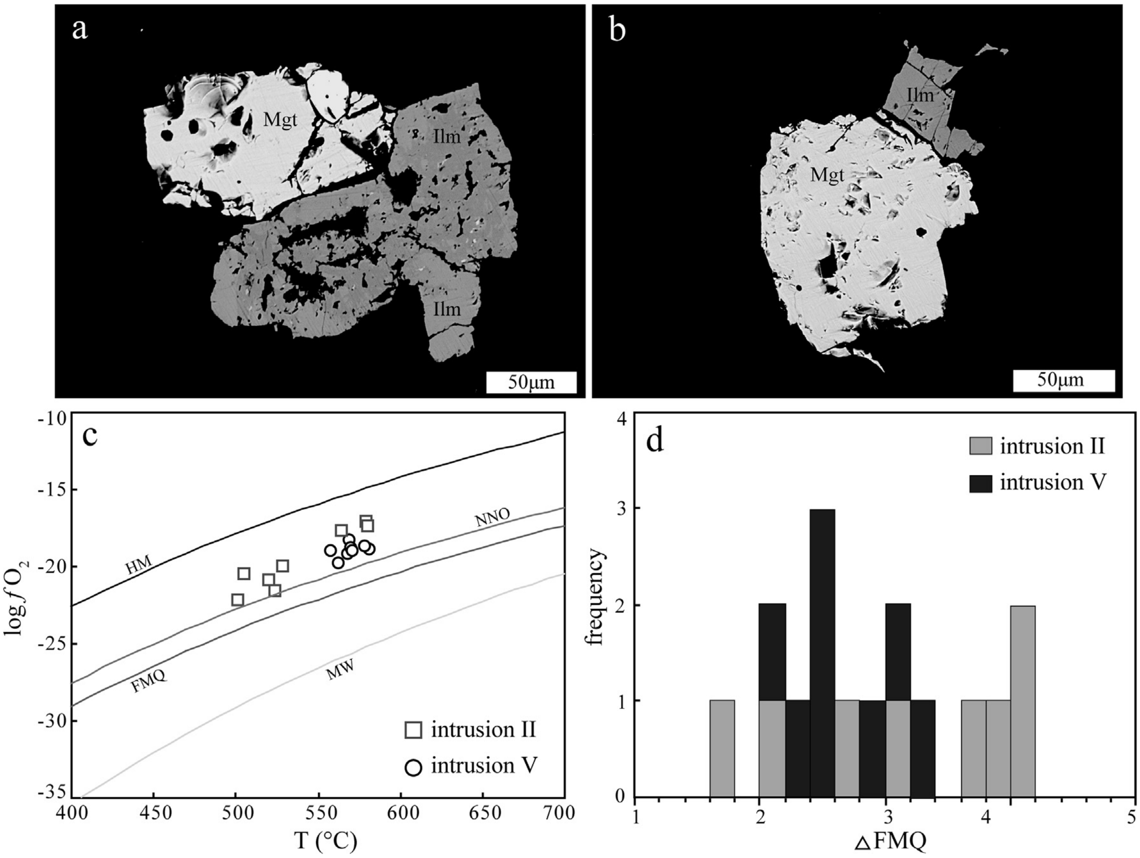

Fig. 8. Backscattered electron (BSE) images show magnetite and ilmenite as intergrowths in the Baogutu intrusions and the estimated oxidation state and temperature. (a–b) Coexisting magnetite and ilmenite with straight boundaries. (c) logfO_2 vs. temperature (at 1kbar). (d) ΔFMQ histogram. ΔFMQ and temperature from magnetite–ilmenite mineral pairs were calculated using ILMAT (Lepage, 2003). HM = hematite–magnetite buffer curve (Spencer and Lindsley, 1981), NNO = nickel– nickel oxide buffer curve (Huebner and Sato, 1970), FMQ = fayalite– magnetite– quartz buffer curve (Huebner, 1971), MW = wustite–magnetite buffer curve (Eugster and Wones, 1962).

matched pairs, which made the results doubtful. Cao et al. (2014) proposed that the logfO_2 value of the Baogutu magma is NNO based on the absence of anhydrite, SO_3 contents in apatite, and whole rock Fe_2O_3/FeO ratios. These authors revaluated the oxidation of the ore-bearing granitoids and identified two distinct logfO_2 values: ΔNNO + 0.6 from zircon Ce anomaly and < NNO + 0 from biotite Fe^{3+}/Fe^{T} ratios (Cao et al., 2017). Our data indicate that the average logfO_2 value for the Baogutu ore-forming magma is ΔFMQ + 2.5 (amphibole Mg* oxygen-barometer) or ΔFMQ + 2.7 (magnetite–ilmenite oxygen-barometer). Both these values exceed the lower limit of logfO_2 value for most porphyry copper porphyries (> ΔFMQ + 2; Mungall, 2002; Richards, 2003; Sun et al., 2013; Hattori, 2018). Therefore, we suggest that the Baogutu deposit is a moderately oxidized porphyry copper deposit.

8.3. Metallogenic implication

Magmatic oxidation state plays an important role in the speciation and solubility of sulfur in silicate melts, which in turn influences the solubility of chalcophile and siderophile elements (Nadeau et al., 2010; Jugo et al., 2010; Botcharnikov et al., 2011). Shen et al. (2015) suggested a positive correlation between logfO_2 values and the scale of the deposits based on oxygen fugacity data of porphyry deposits in the Balkhash–Junggar metallogenic belts. Zhang et al. (2017) combined the zircon Ce^{4+}/Ce^{3+} ratios with copper reserves of seven porphyry deposits worldwide and reached a similar conclusion.

The Baogutu intrusions show obvious differences in mineralization styles. The intrusions I, II and IV developed a small amount of disseminated pyrite and chalcopyrite. The intrusion III was moderately mineralized with a variety of sulfides. The intrusion V contains plenty of disseminated and vein-type sulfides. However, there is no obvious correlation between their oxygen fugacity and mineralization intensity. The least mineralized intrusion II has a high average logfO_2 value of ΔFMQ + 2.8 based on amphibole compositions, moderate zircon Ce^{4+}/Ce^{3+} ratio (82.5) and Eu/Eu* ratio (0.38). The moderately mineralized intrusion III has the lowest average logfO_2 value (ΔFMQ + 2.1 based on amphibole compositions), the highest zircon Ce^{4+}/Ce^{3+} ratio (115.8) and Eu/Eu* ratio (0.47). The strongly mineralized intrusion V has a moderate logfO_2 value of ΔFMQ + 2.6 based on amphibole compositions. This intrusion also has moderate zircon Ce^{4+}/Ce^{3+} ratio (average 69.1) and Eu/Eu* ratio (average 0.48). The logfO_2 values of the intrusion II increased with decreasing temperatures, while those of the intrusion V decreased gradually with decreasing temperatures. This demonstrates that magmatic oxidation state is not responsible for the mineralization diversity among the Baogutu intrusions.

Various processes are vital to the formation of an economic porphyry deposit, from partial melting in the source area, through mechanisms for magma emplacement, to magmatic–hydrothermal fluid evolution in the upper crust. Only optimization of these processes can affect the grade and size of the resulting deposits. The Baogutu mineralized intrusions underwent various degrees of magmatic–hydrothermal evolution (Wei et al., 2014; Zhu et al., 2014; Shen and Pan, 2015; Cao et al., 2016), which may be responsible for their different mineralization intensities.

9. Conclusion

The Baogutu intrusions mainly consist of granodiorite, quartz

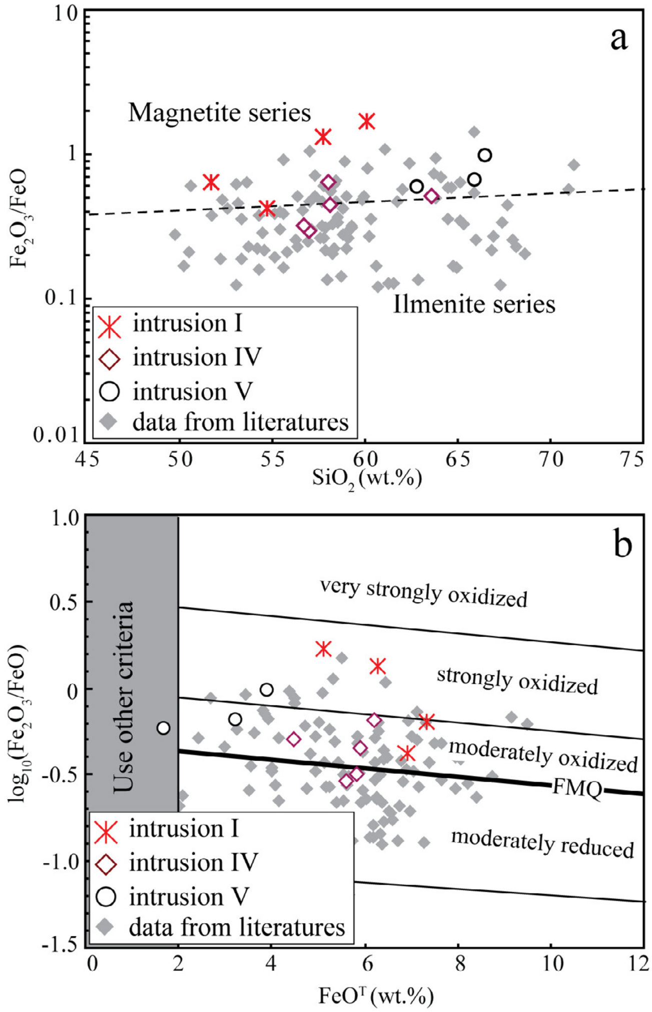

Fig. 9. (a) Whole rock Fe^{3+}/Fe^{2+} ratios vs. silica for the carefully selected fresh samples from the Baogutu intrusions. (b) Log(Fe_2O_3/FeO) vs. FeO (after Blevin, 2004). Literature data from Zhang et al. (2006a), Shen et al. (2009), Shen and Pan (2013) and Cao et al. (2016).

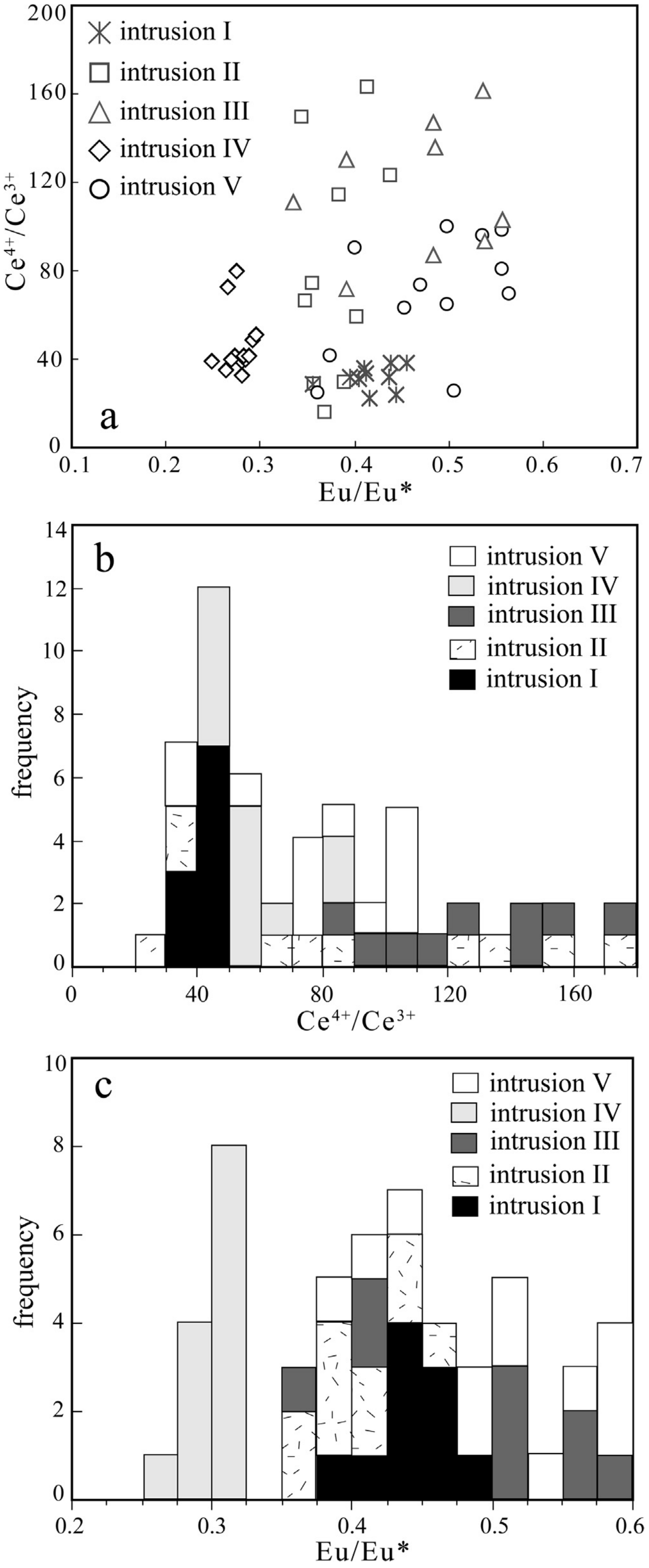

Fig. 10. Zircon trace element ratio plots and concentration histograms for the Baogutu intrusions. (a) Zircon Ce^{4+}/Ce^{3+} vs. Eu/Eu*. (b) Zircon Ce^{4+}/Ce^{3+} ratio histogram. (c) Zircon Eu/Eu* ratio histogram.

diorite and diorite, with a small amount of pyroxene diorite. As the accessory mineral phases, magnetite and ilmenite occur as inclusions in amphibole and biotite, or as interstitial minerals among amphibole, plagioclase and biotite. The intrusions I and II contain more abundant magnetite compared to ilmenite, while the intrusions III and IV only contain ilmenite. Ilmenite is more popular compared with magnetite in the intrusion V. Fresh samples with whole-rock Fe^{3+}/Fe^{2+} ratios of 0.29 – 0.98 plot along the boundary between magnetite series and ilmenite series. Magnetite–ilmenite mineral pairs record logfO_2 values varying from ΔFMQ + 1.6 to ΔFMQ + 3.9. Amphibole compositions provide logfO_2 values of △FMQ + 1.7 to ΔFMQ + 3.5. Zircon Ce^{4+}/Ce^{3+} ratios (15.9 – 163) and Eu/Eu* ratios (0.25 – 0.57) plot in the range of typical porphyry copper deposits worldwide. Present study suggests that the Baogutu ore-forming magma is oxidized with logfO_2 value of ΔFMQ + 2.5 (based on amphibole oxygen-barometer) or ΔFMQ + 2.7 (based on magnetite–ilmenite oxygen-barometer), indicating a moderately oxidized magmatic condition for porphyry copper ore-formation.

Acknowledgements

This work is financially supported by Natural Science Foundation of China (Nos. 41403033, 41602212, 41502107, 41672047). We would like to express our gratitude to Dr. Haochen Yu, Kunfeng Qiu, Huichao

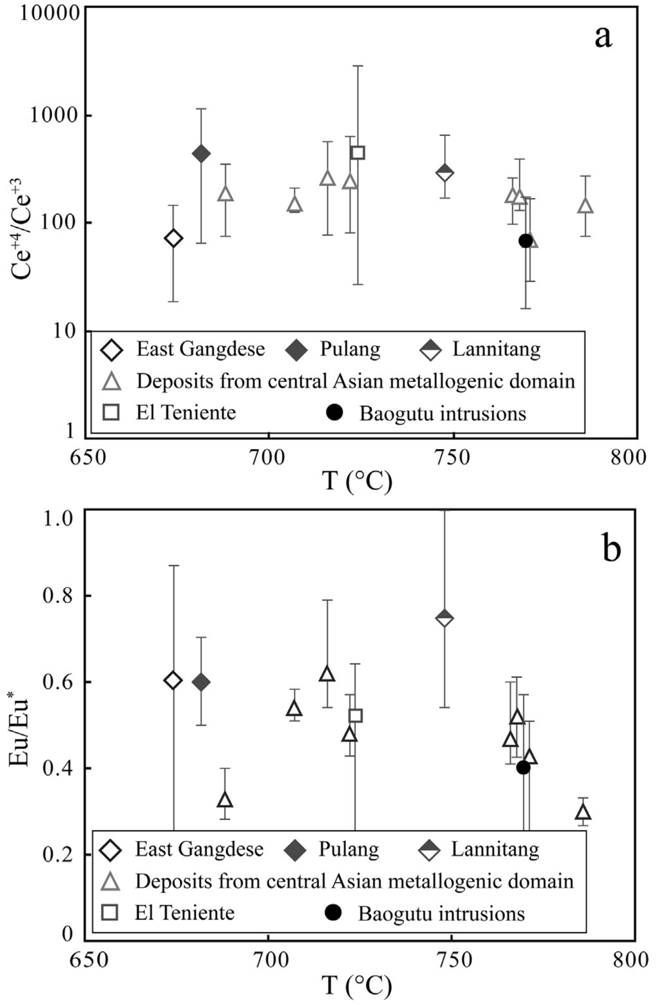

Fig. 11. Zircon trace element ratio and temperature diagrams for porphyry copper deposits worldwide. (a) Zircon Ce^{4+}/Ce^{3+} vs. temperature; (b) Zircon Eu/Eu^{*} vs. temperature. Temperature was calculated using the Ti-in-zircon thermometer based on Ferry and Watson (2007). Data from this study as well as from literatures (Muñoz et al., 2012; Wang et al., 2014; Shen et al., 2015; Kong et al., 2016; Yu et al., 2016).

Zhang and three anonymous reviewers for providing detailed comments and suggestions, which helped us to improve this manuscript greatly.

Appendix A. Supplementary data

Supplementary data to this article can be found online at https://doi.org/10.1016/j.oregeorev.2019.02.018.

References

An, F., Zhu, Y.F., 2009. Significance of native arsenic in the Baogutu gold deposit, Western Junggar, Xinjiang, NW China. Chinese Sci. Bull. 54, 1744–1749.

An, F., Zhu, Y.F., 2010. Native antimony in the Baogutu gold deposit (west Junggar, NW China): its occurrence and origin. Ore Geol. Rev. 37, 214–223.

Andersen, D.J., Lindsley, D.H., 1985. New (and final!) models for the Ti-magnetite/ilmenite geothermometer and oxygen barometer. Abstract AGU 1985 Spring Meeting Eos Transactions 46, 416.

Anderson, J.L., Barth, A., Wooden, J.L., Mazdab, F., 2008. Thermometers and thermobarometers in granitic systems. Rev. Mineral. Geochem. 69, 121–142.

Audétat, A., Pettke, T., 2006. Evolution of a porphyry-Cu mineralized magma system at Santa Rita, New Mexico (USA). J. Petrol. 47, 2021–2046.

Audétat, A., Pettke, T., Dolejš, D., 2004. Magmatic anhydrite and calcite in the ore-forming quartz monzodiorite magma at Santa Rita, New Mexico (USA): genetic constraints on porphyry-Cu mineralization. Lithos 72, 147–161.

Ballard, J.R., Palin, J.M., Campbell, I.H., 2002. Relative oxidation states of magmas inferred from Ce(IV)/Ce(III) in zircon: application to porphyry copper deposits of northern Chile. Contrib. Mineral. Petrol. 144, 347–364.

Bao, X.S., Yang, L.Q., He, W.Y., Gao, X., 2018. Importance of magmatic water content and oxidation state for porphyry-style Au mineralization: an example from the giant Beiya Au deposit, SW China. Minerals 8, 441–453.

Blevin, P.L., 2004. Redox and compositional parameters for interpreting the granitoid metallogeny of eastern Australia: implications for gold-rich ore system. Resour. Geol. 54, 241–252.

Blundy, J., Wood, B., 1994. Prediction of crystal-melt partition coefficients from elastic moduli. Nature 372, 452–454.

Botcharnikov, R.E., Linnen, R.L., Holtz, W.M., Jugo, P.J., Berndt, J., 2011. High gold concentrations in sulphide-bearing magma under oxidizing conditions. Nat. Geosci. 4, 112–115.

Brett, R., Sato, M., 1984. Intrinsic oxygen fugacity measurements on seven chondrites, a pallasite, and a tektite and the redox state of meteorite parent bodies. Geochim. Cosmochim. Acta 48, 11–120.

Buddington, A.F., Lindsley, D.H., 1964. Iron–titanium oxide minerals and synthetic equivalents. J. Petrol. 5, 310–357.

Burnham, A.D., Berry, A.J., 2012. An experimental study of trace element partitioning between zircon and melt as a function of oxygen fugacity. Geochim. Cosmochim. Acta 95, 196–212.

Cannell, J., Cooke, D.R., Walshe, J.L., Stein, H., 2005. Geology, mineralization, alteration, and structural evolution of the El Teniente porphyry Cu–Mo deposit. Econ. Geol. 100, 979–1003.

Cao, M.J., Evans, N., Hollings, P., Cook, D.R., Mclnnes, B.I.A., Qin, K.Z., Li, G.M., 2018. Phenocryst zonation in porphyry-related rocks of the Baguio district, Philippines: evidence for magmatic and metallogenic processes. J. Petrol. 59, 825–848.

Cao, M.J., Qin, K.Z., Li, G.M., Jin, L.Y., Evans, N.J., Yang, X.R., 2014. Baogutu: an example of reduced porphyry Cu deposit in western Junggar. Ore Geol. Rev. 56, 159–180.

Cao, M.J., Qin, K.Z., Li, G.M., Evans, N.J., Hollings, P., Lu, Y.J., 2016. Genesis of ilmenite-series I-type granitoids at the Baogutu reduced porphyry Cu deposit, western Junggar, NW China. Lithos 246–247, 13–30.

Cao, M.J., Qin, K.Z., Li, G.M., Evans, N.J., Hollings, P., Maisch, M., Kappler, A., 2017. Mineralogical evidence for crystallization conditions and petrogenesis of ilmenite-series I-type granitoids at the Baogutu reduced porphyry Cu deposit (Western Junggar, NW China): Mossbauer spectroscopy, EPM and LA-(MC)-ICPMS analyses. Ore Geol. Rev. 86, 382–403.

Carroll, M.K., Rutherford, M.J., 1988. Sulfur speciation in hydrous experimental glasses of varying oxidation state: results from measured wavelength shifts of sulfur X-rays. Am. Mineral. 73, 845–849.

Chen, B., Zhu, Y.F., 2011. Petrology, geochemistry and zircon U-Pb chronology of gabbro in Darbut ophiolitic mélange, Xinjiang. Acta Petrol. Sin. 27, 1746–1758 (in Chinese with English abstract).

Eugster, H.P., Wones, D.R., 1962. Stability relations of the ferruginous biotite, annite. J. Petrol. 3, 82–125.

Ferry, J.M., Watson, E.B., 2007. New thermodynamic models and revised calibrations for the Ti-in-zircon and Zr-in-rutile thermometers. Contrib. Mineral. Petr. 154, 429–437.

Foster, M.D., 1960. Interpretation of composition of trioctahedral micas. Geol. Surv. Prof. Paper 354B, 11–49.

Ghiorso, M.S., Evans, B.W., 2008. Thermodynamics of rhombohedral oxide solid solutions and a revision of the Fe–Ti two-oxide geothermometer and oxygenbarometer. Am. J. Sci. 308, 957–1039.

Ghiorso, M.S., Sack, R.O., 1991. Fe–Ti oxide geothermometry: thermodynamic formulation and the estimation of intensive variables in silicic magmas. Contrib. Mineral. Petr. 108, 485–510.

Grondahl, C., Zajaca, Z., 2017. Magmatic controls on the genesis of porphyry Cu–Mo–Au deposits: the Bingham Canyon example. Earth. Planet. Sci. Lett. 480, 53–65.

Grove, T.L., Elkins-Tanton, L.T., Parman, S.W., Müntener, O., Gaetani, G.A., 2003. Fractional crystallization and mantle melting controls on calcalkaline differentiation trends. Contrib. Mineral. Petr. 145, 515–533.

Han, B.F., Ji, J.Q., Song, B., Chen, L.H., Zhang, L., 2006. Late Paleozoic vertical growth of continental crust around the Junggar Basin, Xinjiang, China (part 1): timing of post collisional plutonism. Acta Petrol. Sin. 22, 1077–1086 (in Chinese with English abstract).

Hattori, K., 2018. Porphyry copper potential in Japan based on magmatic oxidation state. Resour. Geol. 68 (2), 126–137.

Hattori, K.H., Keith, J.D., 2001. Contribution of mafic melt for porphyry deposits: evidence from Pinatubo and Bingham. Miner. Deposita. 36, 799–806.

Hou, Z.Q., Ma, H.W., Zaw, K., Zhang, Y.Q., Wang, M.J., Wang, Z., Pan, G.T., Tang, R.L., 2003. The Himalayan Yulong poyphyry copper belt: production of large-scale strike-slip faulting in Eastern Tibet. Econ. Geol. 98, 125–145.

Huebner, J.S., 1971. Buffering techniques for hydrostatic systems at elevated pressure. Research techniques for high pressure and high temperature. Springer Berlin Heidelberg, New York, pp. 123–177.

Huebner, J.S., Sato, M., 1970. The oxygen fugacity-temperature relationships of manganese oxide and nickel oxide buffers. Am. Miner. 55, 934–952.

Idrus, A., Kolb, J., Meyer, F.M., 2007. Chemical composition of rock forming minerals in copper–gold-bearing tonalite porphyries at the Batu Hijau deposit, Sumbawa island, Indonesia: implications for crystallization conditions and fluorine-chlorine fugacity. Resour. Geol. 57, 102–113.

Irvine, T.N., Baragar, W.R.A., 1971. Guide to chemical classification of common volcanic rocks. Can. J. Earth. Sci. 8, 523–548.

Jenner, F.E., O'Neill, H.S.C., Arculus, R.J., Mavrogenes, J.A., 2010. The magnetite crisis in the evolution of arc-related magmas and the initial concentration of Au, Ag and Cu. J. Petrol. 51, 2445–2464.

Jiang, J.Y., Zhu, Y.F., 2018. Characterization of anhydrous to hydrous paragenetic sequence from pyroxene-bearing and pyroxene-absent variants of the late Carboniferous Baobei pluton in west Junggar of China. Gondw. Res. 63, 129–151.

Jugo, P., Luth, R., Richards, J., 2005. Experimental data on the speciation of sulfur as a function of oxygen fugacity in basaltic melt. Geochim. Cosmochim. Acta 69, 497–503.

Jugo, P.J., Wilke, M., Botcharnikov, R.E., 2010. Sulfur K-edge XANES analysis of natural and synthetic basaltic glasses: implications for S speciation and S content as function of oxygen fugacity. Geochim. Cosmochim. Acta 74, 5926–5938.

Khashgerel, B.E., Kavalieris, I., Hayashi, K., 2008. Mineralogy, textures and whole-rock geochemistry of advanced argillic alteration: Hugo Dummett porphyry Cu–Au deposit, Oyu Tolgoi mineral district, Mongolia. Miner. Deposita. 43, 913–932.

Khashgerel, B.E., Rye, R.O., Hedenquist, J.W., Kavalieris, I., 2006. Geology and reconnaissance stable isotope study of the Oyu Tolgoi porphyry Cu–Au system, South Gobi, Mongolia. Econ. Geol. 100, 503–522.

Kong, D.X., Xu, J.F., Chen, J.L., 2016. Oxygen isotope and trace element geochemistry of zircons from porphyry copper system: implications for Late Triassic metallogenesis within the Yidun Terrane, southeastern Tibetan Plateau. Chem. Geol. 441, 148–161.

Leake, B.E., Woolley, A.R., Arps, C.E.S., Birch, W.D., Gilbert, M.C., Grice, J.D., Hawthorne, F.C., Kato, A., Kisch, H.J., Krivovichev, V.G., Linthout, K., Laird, J., Mandarino, J., Maresch, W.V., Nickel, E.H., Rock, N.M.S., Schumacher, J.C., Smith, D.C., Stephenson, N.C.N., Ungaretti, L., Whittaker, E.J.W., Youzhi, G., 1997. Nomenclature of amphiboles: report of the Subcommittee on Amphiboles of the International Mineralogical Association Commission on new minerals and mineral names. Mineral. Mag. 61, 295–321.

Lepage, L.D., 2003. ILMAT: an Excel worksheet for ilmenite–magnetite geothermometry and geobarometry. Comput. Geosci. 29, 673–678.

Li, X.Z., Han, B.F., Ji, J.Q., Li, Z.H., Liu, Z.Q., Yang, B., 2004. Geology, geochemistry and K-Ar ages of the Karamay basic–intermediate dyke swarm from Xinjiang, China. Geochimica 33, 574–584 (in Chinese with English abstract).

Liang, H.Y., Campbell, I.H., Allen, C., Sun, W.D., Liu, C.Q., Yu, H.X., Xie, Y.W., Zhang, Y.Q., 2006. Zircon Ce^{4+}/Ce^{3+} ratios and ages for Yulong ore-bearing porphyries in eastern Tibet. Miner. Deposita. 41, 152–159.

Liang, H.Y., Sun, W., Su, W.C., Zartman, R.E., 2009. Porphyry Copper-Gold mineralization at Yulong, China, promoted by decreasing redox potential during magnetite alteration. Econ. Geol. 104, 587–596.

Liu, Y.L., Guo, L.S., Song, H.X., Song, B., Zhang, R., Xu, F.J., Zhang, Y.X., 2009. Geochronology of Baogutu porphyry copper deposit in Western Junggar area, Xinjiang of China. Sci. China. Ser. D: Earth. Sci. 52, 1543–1549.

Middlemost, E.A.K., 1994. Naming materials in the magma/igneous rock system. Earth. Sci. Rev. 37, 215–224.

Mungall, J.F., 2002. Roasting the mantle: slab melting and the genesis of major Au and Au-rich deposits. Geology 30, 915–918.

Muñoz, M., Charrier, R., Fanning, C.M., Maksaev, V., Deckart, K., 2012. Zircon trace element and O-Hf isotope analyses of mineralized intrusions from El Teniente ore deposit, Chilean Andes: constraints on the source and magmatic evolution of porphyry Cu–Mo related magmas. J. Petrol. 53, 1091–1122.

Nadeau, O., Williams-Jones, A.E., Stix, J., 2010. Sulphide magma as a source of metals in arc-related magmatic hydrothermal ore fluids. Nat. Geosci. 3, 501–505.

Patricio, C.C., Gonzalo, R.S., 2001. Oxide mineralization at the Radomiro Tomic porphyry copper deposit, Northern Chile. Econ. Geol. 96, 387–400.

Pearce, N.J.G., Perkins, W.T., Westgate, J.A., Gorton, M.P., Jackson, S.E., Neal, C.R., Chenery, S.P., 1997. A compilation of new and published major and trace element data for NIST SRM 610 and NIST SRM 612 glass reference materials. Geostand. Geoanal. Res. 21, 115–144.

Pichavant, M., Martel, C., Bourdier, J.L., Scaillet, B., 2002. Physical conditions, structure, and dynamics of a zoned magma chamber: Mount Pelee (Martinique, Lesser Antilles Arc). J. Geophys. Res. 107 (B5) ECV 1–1–ECV 1–28.

Qiu, T., Zhu, Y.F., 2015. Geology and geochemistry of listwaenite-related gold mineralization in Sayi gold deposit, Xinjiang, NW China. Ore Geol. Rev. 70, 61–79.

Randall, J.A., Saldana, E.A., Clark, K.F., 1994. Exploration in a volcano–plutonic center at Guanajuato, Mexico. Econ. Geol. 89, 1722–1751.

Rhodes, J.M., Vollinger, M.J., 2005. Ferric/ferrous ratios in 1984 Mauna Loa lavas: a contribution to understanding the oxidation state of Hawaiian magmas. Contrib. Mineral. Petr. 149, 666–674.

Richards, J.P., 2003. Tectono–magmatic precursors for porphyry Cu–(Mo–Au) deposit Formation. Econ. Geol. 98, 1515–1533.

Richards, J.P., 2009. Postsubduction porphyry Cu–Au and epithermal Au deposits: products of remelting of subduction-modified lithosphere. Geology 37, 247–250.

Rickwood, P.C., 1989. Boundary lines within petrologic diagram which use oxides of major and minor elements. Lithos 22, 247–263.

Ridolfi, F., Puerini, M., Renzulli, A., Menna, M., Toulkeridis, T., 2008. The magmatic feeding system of El Reventador volcano (Sub-Andean zone, Ecuador) constrained by texture, mineralogy and thermobarometry of the 2002 erupted products. J. Volcanol. Geoth. Res. 176, 94–106.

Ridolfi, F., Renzulli, A., Puerini, M., 2010. Stability and chemical equilibrium of amphibole in calc-alkaline magmas: an overview, new thermobarometric formulations and application to subduction-related volcanoes. Contrib. Mineral. Petr. 160, 45–66.

Rowins, S.M., 2000. Reduced porphyry copper–gold deposits: a new variation on an old theme. Geology 28, 491–494.

Rowins, S.M., Groves, D.I., McNaughton, N.J., Palmer, M.R., Eldridge, C.S., 1997. A reinterpretation of the role of granitoids in the genesis of Neoproterozoic gold mineralization in the Telfer dome, Western Australia. Econ. Geol. 92, 133–160.

Sauerzapf, U., Lattard, D., Burchard, M., Engelmann, R., 2008. The titano magnetite–ilmenite equilibrium: new experimental data and thermooxybarometric application to the crystallisation of basic to intermediate rocks. J. Petrol. 49, 1161–1185.

Scaillet, B., Evans, B.W., 1999. The 15 June 1991 eruption of Mount Pinatubo; I, Phase equilibria and pre-eruption P-T-fO$_2$-fH$_2$ conditions of the dacite magmas. J. Petrol. 40, 381–411.

Schmidt, M.W., 1992. Amphibole composition in tonalite as a function of pressure; an experimental calibration of the Al-in hornblende barometer. Contrib. Mineral. Petr. 110, 304–310.

Shen, P., Shen, Y., Liu, T., Meng, L., Dai, H.W., Yang, Y.H., 2009. Geochemical signature of porphyries in the Baogutu porphyry copper belt, western Junggar, NW China. Gondwana Res. 16, 227–242.

Shen, P., Pan, H.D., 2013. Country-rock contamination of magmas associated with the Baogutu porphyry Cu deposit, Xinjiang, China. Lithos 177, 451–469.

Shen, P., Hattori, K., Pan, H., Jackson, S., Seitmuratova, E., 2015. Oxidation condition and metal fertility of granitic magmas: zircon trace-element data from porphyry Cu deposits in the Central Asian Orogenic Belt. Econ. Geol. 110, 1861–1878.

Shen, P., Pan, H.D., 2015. Methane origin and oxygen-fugacity evolution of the Baogutu reduced porphyry Cu deposit in the West Junggar terrain, China. Miner. Deposita 50, 967–986.

Sillitoe, R.H., 2010. Porphyry copper system. Econ. Geol. 105, 3–41.

Sillitoe, R.H., 2018. Why no porphyry copper deposits in Japan and South Korea? Resour. Geol. 68 (2), 107–125.

Sisson, T.W., Grove, T.L., 1993. Temperature and H_2O contents of low-MgO high-alumina basalts. Contrib. Mineral. Petr. 113, 167–184.

Smith, C.M., Canil, D., Rowins, S.M., Friedman, R., 2012. Reduced granitic magmas in an arc setting: the Catface porphyry Cu-Mo deposit of the Paleogene Cascade Arc. Lithos 154, 361–373.

Smythe, D.J., Brenan, J.M., 2015. Cerium oxidation state in silicate melts: combined fO$_2$, temperature and compositional effects. Geochim. Cosmochim. Acta 170, 173–187.

Smythe, D.J., Brenan, J.M., 2016. Magmatic oxygen fugacity estimated using zircon-melt partitioning of cerium. Earth. Planet. Sci. Lett. 453, 260–266.

Song, H.X., Liu, Y.L., Qu, W.J., Song, B., Zhang, R., Cheng, Y., 2007. Geological characters of Baogutu porphyry copper deposit in Xinjiang, NW China. Acta Petrol. Sin. 23, 1981–1988 (in Chinese with English abstract).

Spencer, K.J., Lindsley, D.H., 1981. A solution model for coexisting irontitanium oxides. Am. Mineral. 66, 1189–1201.

Stern, C.R., Funk, J.A., Skewes, M.A., Arevalo, A., 2007. Magmatic anhydrite in plutonic rocks at the El Teniente Cu–Mo deposit, Chile and the role of sulfur and copper-rich magmas in its formation. Econ. Geol. 102, 1335–1344.

Sun, S.S., McDonough, W.F., 1989. Chemical and isotopic study of oceanic basalts: implications for mantle composition and processes. Geol. Soc. 42, 313–345. London, Special Publications.

Sun, W.D., Liang, H.Y., Ling, M.X., Zhan, M.Z., Ding, X., Zhang, H., Yang, X.Y., Li, Y.L., Ireland, T.R., Wei, Q.R., Fan, W.M., 2013. The Link between reduced porphyry copper deposits and oxidized magmas. Geochim. Cosmochim. Acta 103, 263–275.

Tang, G.J., Wang, Q., Wyman, D.A., Li, Z.X., Zhao, Z.H., Jia, X.H., Jiang, Z.Q., 2010. Ridge subduction and crustal growth in the Central Asian Orogenic Belt: evidence from Late Carboniferous adakites and high-Mg diorites in the western Junggar region, northern Xinjiang (west China). Chem. Geol. 277, 281–300.

Trail, D., Watson, E.B., Tailby, N.D., 2011. The oxidation state of Hadean magmas and implications for early Earth's atmosphere. Nature 480, 79–82.

Venezky, D.Y., Rutherford, M.J., 1999. Petrology and Fe–Ti oxide reequilibration of the 1991 Mount Unzen mixed magma. J. Volcanol. Geoth. Res. 89, 213–230.

Wang, L., Zhu, Y.F., 2015. Multi-stage pyrite and hydrothermal mineral assemblage of the Hatu gold district (west Junggar, Xinjiang, NW China): implications for metallogenic evolution. Ore Geol. Rev. 69, 243–267.

Wang, R., Richards, J.P., Hou, Z.Q., Yang, Z.M., Gou, Z.B., Dufrane, S.A., 2014. Increasing magmatic oxidation state from Paleocene to Miocene in the eastern Gangdese belt, Tibet: implication for collision-related porphyry Cu–Mo ± Au mineralization. Econ. Geol. 109, 1943–1965.

Wang, R., Zhu, Y.F., 2007. Geology of Baobei gold deposit in western Junggar and zircon SHRIMP age of its wall-rock, Western Junggar (Xinjiang, NW China). Geol. J. China Uni. 13, 590–602 (in Chinese with English abstract).

Wei, S.N., Cheng, J.F., Yu, D.B., Zheng, B., Zhu, Y.F., 2011. Petrology and SHRIMP zircon ages of intrusive body III in Baogutu area, Xinjiang. Earth Sci. Front. 18, 212–222 (in Chinese with English abstract).

Wei, S.N., Zhu, Y.F., 2015. Petrology, geochronology and geochemistry of intermediate–acidic intrusions in Baogutu area, west Junggar, Xinjiang. Acta Petrol. Sin. 31, 143–160 (in Chinese with English abstract).

Wei, S.N., Zhu, Y.F., An, F., 2014. Mineralization and elements migration of porphyry copper deposit in Baogutu area, Xinjiang. Miner. Deposits 33, 165–180 (in Chinese with English abstract).

Wilkinson, J.J., 2013. Triggers for the formation of porphyry ore deposits in magmatic arcs. Nat. Geosci. 6, 917–925.

Wones, D.R., Eugster, H.P., 1965. Stability of biotite: experiment, theory, and application. Am. Mineral. 50, 1228–1272.

Xiao, B., Qin, K.Z., Li, G.M., Li, J.X., Xia, D., Chen, L., Zhao, J.X., 2012. Highly oxidized magma and fluid evolution of Miocene Qulong giant porphyry Cu–Mo deposit, Southern Tibet, China. Resour. Geol. 62, 4–18.

Xu, Z., Han, B.F., Ren, R., Zhou, Y.Z., Su, L., 2012. Paleozoic multiphase magmatism at Barleik Mountain, southern West Junggar, Northwest China: implications for tectonic evolution of the West Junggar. Int. Geol. Rev. 55, 633–656.

Yang, G.X., Li, Y.J., Yang, B.K., Zhang, B., Tong, L.L., Santosh, M., 2013. Geochronology and geochemistry of basalts from the Karamay ophiolitic mélange in west Junggar (NW China): implications for Devonian-Carboniferous intra-oceanic accretionary tectonics of the southern Altaids. Geol. Soc. Am. Bull. 125, 401–419.

Yin, J.Y., Long, X.P., Yuan, C., Sun, M., Zhao, G.C., Geng, H.Y., 2013. A Late Carboniferous-Early Permian slab window in the West Junggar of NW China: geochronological and geochemical evidence from mafic to intermediate dikes. Lithos

175–176, 146–162.

Yu, Y.F., Fei, G.C., Li, Y.G., Long, X.R., Tian, E.Y., Liu, G.Q., Lv, F.M., Hua, K.Q., 2016. Oxygen fugacity of intrusions from Lannitang porphyry copper deposit in Zhongdian island arc, Yunnan: implications for mineralization. J. Mineral Petrol. 36, 28–36 (in Chinese with English abstract).

Zajacz, Z., Candela, P.A., Piccoli, P.M., Sanchez-Valle, C., Walle, M., 2013. Solubility and partitioning behavior of Au, Cu, Ag and reduced S in magmas. Geochim. Cosmochim. Acta 112, 288–304.

Zhang, C.C., Sun, W.D., Wang, J.T., Zhang, L.P., Sun, J.S., Wu, K., 2017. Oxygen fugacity and porphyry mineralization: a zircon perspective of Dexing porphyry Cu deposit, China. Geochim. Cosmochim. Acta 206, 343–363.

Zhang, H.C., Zhu, Y.F., 2016. Geology and geochemistry of the Huilvshan gold deposit, Xinjiang, China: implications for mechanism of gold precipitation. Ore Geol. Rev. 79, 218–240.

Zhang, R., Zhang, Y.X., Tong, G.S., Wang, J., Li, L.Q., 2006a. Major breakthrough in copper exploration in the Baogutu porphyry copper deposit, western Junggar, Xinjiang, and its significance. Geol. China 33, 1354–1360 (in Chinese with English abstract).

Zhang, L.C., Wan, B., Jiao, X.J., Zhang, R., 2006b. Characteristics and geological significance of adakitic rocks in copper-bearing porphyry in Baogutu, Western Junggar. Geol. China 33, 626–631 (in Chinese with English abstract).

Zheng, B., Zhu, Y.F., An, F., Huang, Q.Y., Qiu, T., 2015. As–Sb–Bi–Au mineralization in the Baogutu gold deposit, Xinjiang, NW China. Ore Geol. Rev. 69, 17–32.

Zhu, B., Zhang, H.F., Shen, P., Su, B.X., Xiao, Y., He, Y.S., 2018. Redox state of the Baogutu reduced porphyry Cu deposit in the Central Asian Orogenic belt. Ore Geol. Rev. 101, 803–818.

Zhu, Y.F., Xu, X., 2006. The discovery of Early Ordovician ophiolite mélange in Taerbahatai Mts., Xinjiang, NW China. Acta Petrol. Sin. 22, 2833–2842 (in Chinese with English abstract).

Zhu, Y.F., Chen, B., Xin, X., Qiu, T., An, F., 2013. A new geological map of the western Junggar, north Xinjiang (NW China): implications for Paleozoic environmental reconstruction. Episodes 36, 205–220.

Zhu, Y.F., Xu, X., Luo, Z.H., Shen, P., Ma, H.D., Chen, X.H., An, F., Wei, S.N., 2014. Geological Evolution and Ore-Formation in the Core Part of Central Asian Metallogenic Region. Geological. Publishing House, Beijing, pp. 1–202 (in Chinese with English abstract).

Zhu, Y.F., Chen, B., Qiu, T., 2015. Geology and geochemistry of the Baijiantan-Baikouquan ophiolitic mélanges: implications for geologic evolution of west Junggar, Xinjiang, NW China. Geol. Mag. 152, 41–69.

Zhu, Y.F., An, F., Feng, W.Y., Zhang, H.C., 2016. Geological evolution and huge ore-forming belts in the core part of the central Asian metallogenic region. J. Earth Sci. 27, 491–506.

Zou, X.Y., Qin, K.Z., Han, X.L., Li, G.M., Evans, N.J., Li, Z.Z., Yang, W., 2019. Insight into zircon REE oxy-barometers: A Lattice strain model perspective. Earth. Planet. Sci. Lett. 506, 87–96.